

***pH Sensitivity of Electrically Conductive Polypyrrole via Oxidative  
Chemical Vapor Deposition***

*University of Groningen  
14th of April, 2023*

*Supervisors:*

*Prof Dr Ranjita K. Bose*

*Dr Ajay G.P. Kottapalli*

*PhD supervision of Adrivit Mukherjee*

*Job H.T. Schoenmaker*

*S3372995*

## ***Abstract***

Electrically conductive polypyrrole is synthesized through oxidative chemical vapor deposition (oCVD). oCVD processability is demonstrated by the fabrication of an electrospun fiber mat deposited with polypyrrole. It is shown that polypyrrole is sensitive to pH. oCVD parameters and substrates are tested for pH sensing performance and oCVD is additionally investigated for substrate independence. The limit of detection (LOD) of polypyrrole-based material for pH sensing was found to be competitive with glass-electrode pH sensors at 0.007 pH unit. The chemical changes of polypyrrole as a result of pH exposure are analyzed and correlated to the electrical conductive changes observed. The deprotonation due to pH exposure is followed by various analyzation techniques where the influence of the polaron units, bipolaron units and dopant level in the polymer chains related to electrical conductivity is showcased. XPS analysis indicates deprotonation of polypyrrole by pH exposure occurs through the removal of bipolaron and polaron units from the polypyrrole chain. Infrared spectra of oCVD polypyrrole show a particularly distinctive polaron and bipolaron band splitting with deprotonation. This effect suggests a relation of the ratio of polaron and bipolaron band absorption to the deprotonation and is displayed by an effective polaron contribution parameter.

<b>Abstract</b>	<b>1</b>
<b>Introduction</b>	<b>3</b>
1.1. Conjugated Polymers	3
1.2. Oxidative Chemical Vapor Deposition (oCVD)	4
1.3. pH sensing of Conducting Polymers	7
<b>Materials and methods</b>	<b>12</b>
2.1. Materials	12
2.2. Substrate independence	13
Spin Coating	13
2.3. Sensing material production	13
Electrospinning	13
2.4. Structural Analysis	14
Ultraviolet-Visible Spectroscopy (UV-Vis)	14
Fourier-Transform Infrared Spectroscopy (FT-IR)	15
X-ray Photoelectron Spectroscopy (XPS)	15
Scanning Electron Microscopy (SEM)	15
2.5. Sensor Performance	16
2.6. Research Aim	18
<b>Results and Discussion</b>	<b>18</b>
3.1. oCVD substrate independence	18
3.2. UV-Vis Analysis	19
3.3. FT-IR Analysis	21
3.4. XPS Analysis	24
3.5. Sensing Material Performance	29
Sensing Material Construction	29
Electrical Resistance Response	32
Detection and Recovery Time	33
pH Sensing Performance	36
<b>Conclusion</b>	<b>36</b>
<b>Future Outlook</b>	<b>37</b>
<b>Acknowledgments</b>	<b>37</b>
<b>Bibliography</b>	<b>38</b>
<b>Appendices</b>	<b>45</b>

# Introduction

## 1.1. Conjugated Polymers

Conducting polymers (CP's), like polypyrrole (PPy), polyaniline, polythiophene and poly-3,4-ethylenedioxythiophene (PEDOT) rely on their conjugated backbone structure for electronic charge carrying capabilities. CP's promote a broad array of applications due to having metal-like capability to conduct electricity while having relevant mechanical property advantages. An array of conducting polymers possess flexibility and stretchability combined with certain CP's being biocompatible [1]. The use of metal-oxide nanoparticles implemented in other materials has been done to achieve similar mechanical properties as CP's. Metal-oxide nanoparticles, however, do not have the required long-term stability of electrical conductivity and reversibility required for several applications. [2-4].

Application areas for CP's are plenty due to the relevant advantages in mechanical properties over their traditional counterparts. Implementation fields for CPs consist of (bio)sensors, supercapacitors, solar cells, nanocoatings and specific catalyst types. Besides biosensors, other biomedical applications like drug delivery systems have been proposed (Figure 1) [5,6].

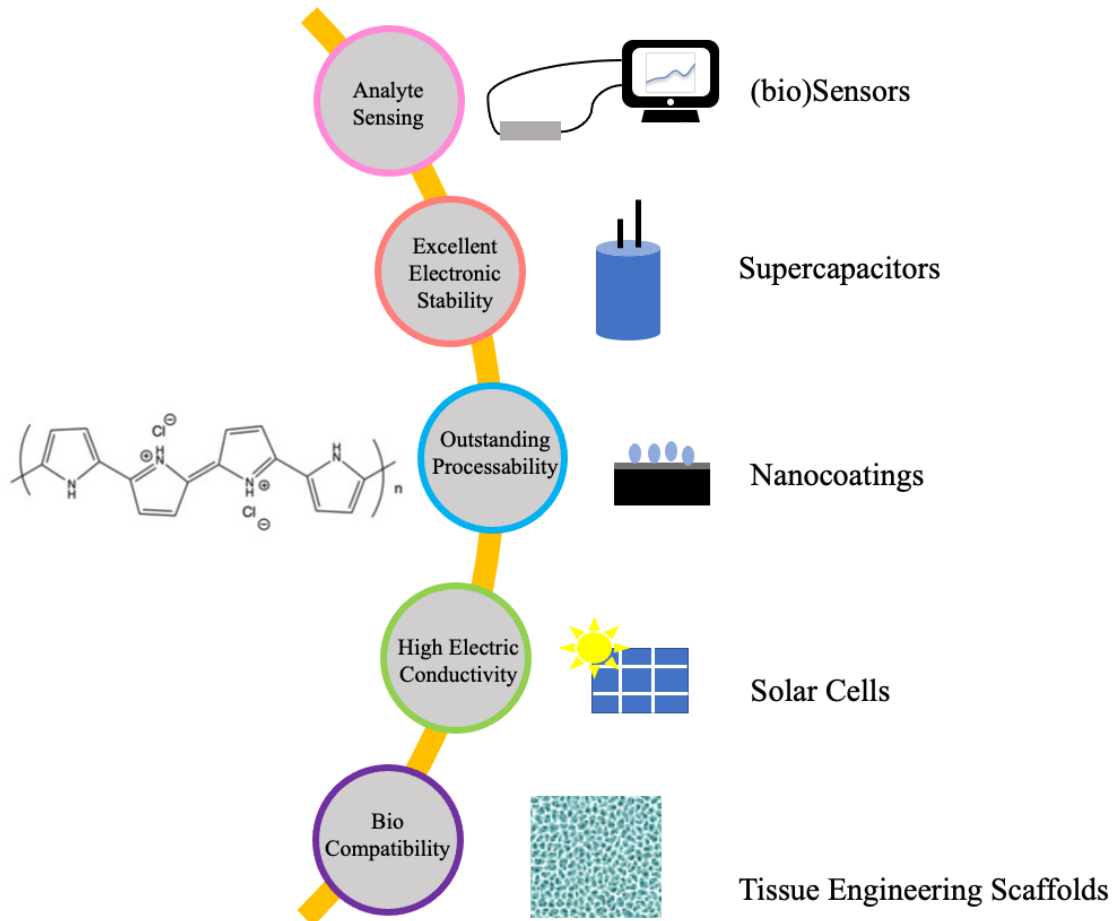


Figure 1: *The variety of application options for CP's showcased. Shown for oCVD processed polypyrrole conjugated bipolaron polymer structure.*

Polypyrrole is one of the classical conjugated polymers systems discovered in 1979 by Diaz *et al.* [7]. Which is in line with the general research trends on conjugated organic polymer systems starting mostly from the 1980's [8]. Conducting polymers such as polypyrrole often exhibit different configurations that affect the resulting electrical properties. The configurations consist of different complexes present in the polymer chains in combination with having a conjugated backbone structure. The complexes that give polypyrrole the ability to conduct electron charge are polaron and bipolaron structures (figure 2). Rearrangement and delocalization of bipolarons lead to the formation of polaron complexes. To improve the stability of the charges in these polaron structures, dopant anions are presented into the polymer system [9]. Polarons act as electron holes in p-type semiconducting and can shift over 8-50 monomer units in a conjugated polymer system, inducing the conductive charge carrying abilities of the polymer structures [10].

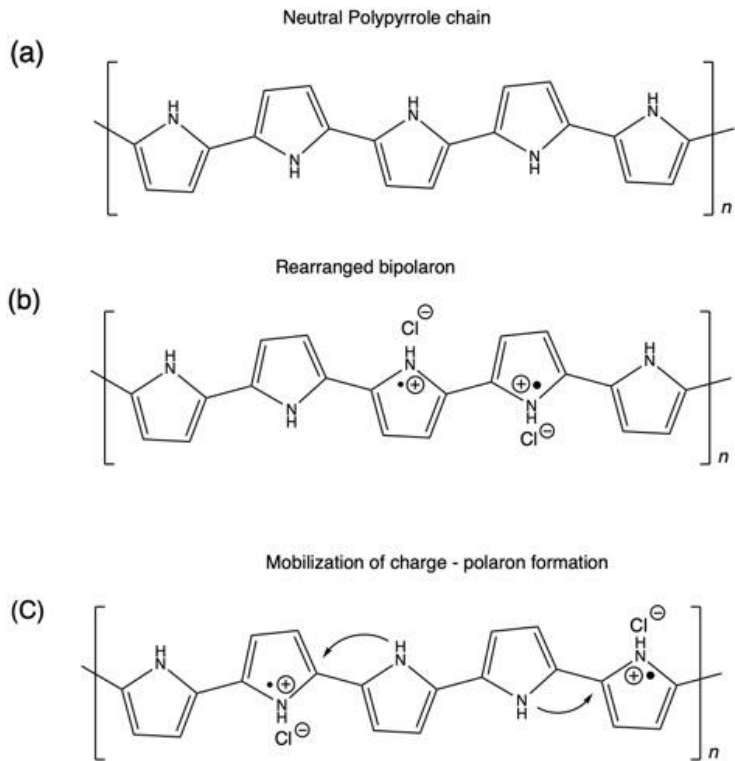


Figure 2: *Neutral non-conducting polypyrrole chain (a). The rearranged bipolaron structure (b) followed by the delocalization of the charge and the formation of polaron structures (c). The rearrangement of the electrons in this bipolaron structure leads to the ability to delocalize the charge along the chain.*

## 1.2 Oxidative Chemical Vapor Deposition (oCVD)

Current conductive polymer synthesis processes mostly rely on electrochemical deposition and solution polymerization [11]. Though successful, solution polymerization for these types of polymers provides drawbacks. Conductive polymers are usually insoluble, mainly due to their long conjugation lengths providing rigid structures [12]. This greatly hinders the processability into tailored applications. Moreover, solution polymerization yields low conductivity CPs where

further doping processing is required [13]. An addition of an extra group to the monomer units or the use of specific solvents or alternative environments is required to improve the solubility [14]. Besides, the conjugation length of CP produced through solution-based processes is low. This negatively impacts the conductivity of the produced CP which is dependent (among other properties) on the conjugation length [15]. Also, thin film formation for solution-based polymerization processes through methods like spin-coating (section 2.2) are impacted by pinhole-formation due to evaporation of solvent through the thin film during drying. This negatively influences the morphology of the polymer film, in turn also affecting the conductivity [16]. The use of substrates is limited due to the surface tension characteristics of the material used. Dewetting or air gap formation can occur with film formation of solution polymerization CP's [17]. Methods to reduce dewetting, like addition of surfactants act as impurities in the CP film, therefore reducing stability and long-term efficiency of the CP film [18].

Oxidative chemical vapor deposition (oCVD) is an alternative polymerization method for the step-growth production of conductive polymer films through the vapor-phase. oCVD is a novel polymerization technique which has gained research traction in the last decade. oCVD is performed in a vacuum chamber. Liquid-state monomer is vaporized and entered into the vacuum chamber. The oxidant can either be a sublimated solid-phase oxidant or a vaporized liquid. Vaporizing a liquid provides additional control over the oxidant feed rate to achieve a desired reactant ratio between the monomer and oxidant feed [19]. The reactant ratio influences the conjugation length and bipolaron concentration in the CP chain and is therefore a crucial parameter to control for achieving the desired conductivity [20]. One of the main advantages of using oCVD to process CP's is that it does not require a polymer in solution, bypassing one of the main issues regarding CP's being the complex solubility of CP's. Besides, the formation of pinholes in the polymer film morphology is not present because no liquid evaporation occurs after film formation. Subsequently, additional conductivity and the ability to decrease the film-thickness to nanometer scale as well as producing ultrasmooth surfaces is possible. The conjugation length is not dependent on the solubility of the polymer complexes in a solvent using oCVD. Therefore, conjugation lengths - and in turn conductivity - can be significantly increased using oCVD polymerization [21]. This research analyzes the substrate independence of oCVD. Because oCVD requires mild substrate temperatures (25-150 degrees Celsius), the use of even delicate substrates for oCVD deposition such as unmodified paper can be performed [22].

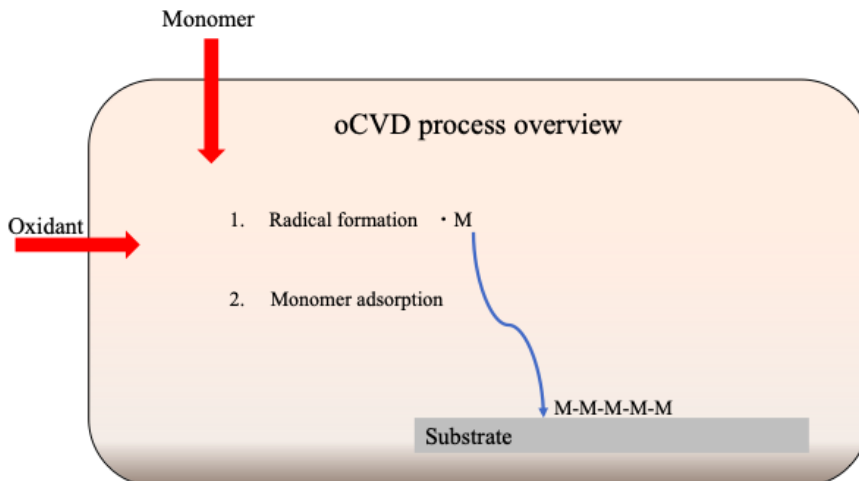


Figure 3: Overview of the oCVD process where oxidant and monomer vapor enter the reaction chamber. The monomer is oxidized and a radical is formed in the monomer structure. This monomer is adsorbed onto the substrate surface where subsequent monomers attach onto the monomer chain providing step-growth polymerization.

The oxidant not only oxidizes the monomer units to form radicals required for the initiation of the reaction, but it also provides dopant ions to the conductive polymer chains. CP's like polypyrrole conduct electricity because of its ability to transport electrons across the polymer chains. This can be done due to the formation of electron holes, also known as polarons. Electron hole charge carrying is known as p-type semiconducting. Polarons can form from the delocalization of bipolarons. These bipolarons are formed in-situ during the oCVD reaction while producing the CP [20] (Figure 4). The exact mechanism of the formation of bipolarons and the subsequent rearrangement to polarons is still open to discussion [23]. The stability of these polarons and bipolarons is greatly increased by the incorporation of doping counter-ions [24]. With the oCVD process, the ratio of monomer and oxidant inflow into the reaction chamber can be controlled. The ability to control the ratio of the presence of monomer and oxidant influences the doping concentration in the CP chains. Subsequently, the ability of oCVD processing to control the ratio of monomer and oxidant gives control over the in-situ doping of the CP chain. The concentration of doping anions in the CP chain has an optimum where the conductivity is maximized [20]. This is because at higher oxidant concentration, the CP chains are overoxidized and conjugation length decreases [21]. The influence of in-situ doping of the formed CP chains is unique to CVD processing.

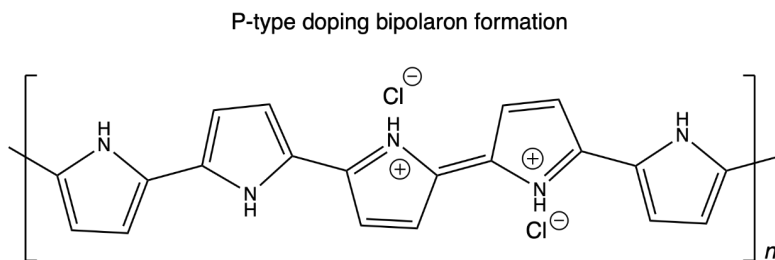


Figure 4: Overview of polypyrrole chain. The oCVD process provides in-situ doping and bipolaron formation of the polypyrrole chain to induce the conductive ability of the polymer chain.

The oCVD method to produce conducting polymers has been successfully performed for an array of different polymers and dopant materials. The discovery of oCVD has been done using the (3,4-ethylenedioxythiophene) monomer to form PEDOT by Lock et al. [25]. After this, the compatibility of oCVD with different polymers and copolymers has been proved including polythiophene (PTh), Polyaniline (PANI) and recently polypyrrole (PPy) [19,20,26]. Different oxidants have been proven to be compatible with the above mentioned monomers.

The proposed mechanism for the formation of a polymer complex using oCVD is schematically explained in Figure 5 for the formation of oCVD polypyrrole. Pyrrole monomer units and  $SbCl_5$  are adsorbed onto the substrate surface where the pyrrole monomer unit is oxidized as an initiation step. This forms a radical and cation in the pyrrole monomer complex (a). Two oxidized

monomer units combine into a bication biradical complex which is deprotonated into a pyrrole dimer (b). Subsequent oxidation of the dimer from the oxidant present in the system gives a new site with a cation and radical (c). This site can react with another oxidized monomer unit to form a 3-monomer unit complex (d). The 3-monomer complex can repeat the steps described in (b) and (c) to form polypyrrole (d) [20].

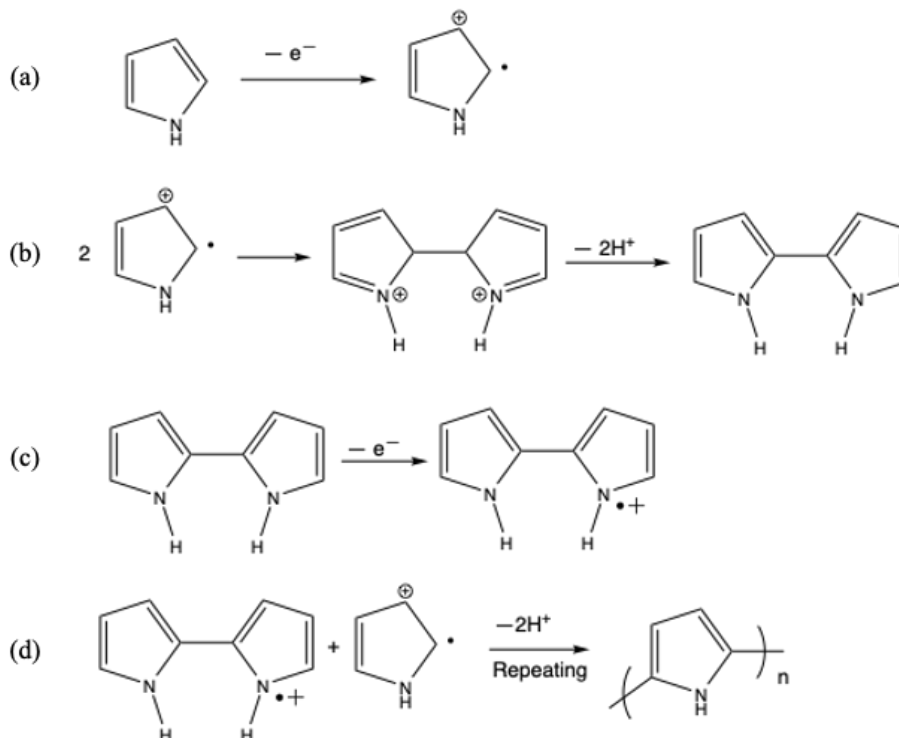


Figure 5: Schematic overview of the reaction mechanism of the step growth formation of polypyrrole as produced by oCVD oxidative polymerization.

### 1.3. pH sensing of Conducting Polymers

With regards to pH biosensing, conductive polymers rely on their intrinsic properties which change because of analyte exposure. The CP's can be analyzed by stimuli induced changes in the electrical or optical properties due to changes in their molecular structure. In the case of pH induced stimuli, polypyrrole undergoes changes in functional properties such as electronic conductivity. There are a variety of methods to analyze these changes of which the four most relevant methods are briefly explained (Table 1).



<i>Measuring method</i>	<i>Method function</i>	<i>Construction of complex</i>
Potentiometric	Voltage difference between working and reference electrode. [27]	<ul style="list-style-type: none"> <li>• CP deposited on an electronic conductor with reference electrode</li> <li>• Voltage meter</li> </ul>
Amperometric	Change of current between working and reference electrode. [28]	<ul style="list-style-type: none"> <li>• CP deposited on an electrode with immobilized enzyme with reference electrode</li> <li>• Current meter</li> </ul>
Conductometric	Change in resistance as a function of CP structural changes. [27]	<ul style="list-style-type: none"> <li>• Polymer thin film</li> <li>• 2-or-4-probe resistance meter</li> </ul>
Colorimetric	Change of color as a result of changing analyte stimuli. [29]	<ul style="list-style-type: none"> <li>• Polymer thin film</li> <li>• Color-analyte calibration</li> </ul>

Table 1: Overview of the methods of measuring analytes in a biosensor application.

Colorimetric pH sensing requires a reading of the diagnostic material in the sensor. The color reading in a colorimetric sensing device is subjective. Because of this, accurate sensing across a long pH range is challenging due to interpretation errors. This makes colorimetric mostly suitable for rough measurements and fast readings. To tackle this subjective sensing method, a method using a smartphone application which analyzes the color of the sensor is proposed [30].

Potentiometric and amperometric sensing methods are fast; however, both require the construction of a relatively complicated setup containing two or more electrodes. The electrodes may need to be coated with enzymes to be correctly modified for sensing capabilities.

Conductometric sensing is a simplified measuring technique and is not selective towards specific ions using a CP sensor without surface modification [31]. Since conductometric sensing relies on changes in the structure of a CP, the detection times are relatively long, in the order of seconds or minutes [32]. Objective reading can be done making it an accurate analyzation method [33].

pH biosensing can be performed on all physiological fluids. The target pH biosensing application will depict which measurement method is best suited. Recent work on pH biosensing has been done by Unger *et al.* [34] on a temporary tattoo sweat pH sensor. Sweat pH was measured by screen printed PEDOT:PSS on a pH dependent swelling hydrogel. Sweat pH sensing gives relevant health information as the composition can be directly correlated to that of blood [35]. Skin-attachable colorimetric pH sweat pH biosensors are also proposed [36].

The determination of pH in saliva can help establish dental health. Miniaturized pH sensors open the possibility for measurement of pH in small-volume liquids. This is especially for pH sensing in physiological fluids where low sample volumes can be extracted. A potentiometric miniaturized pH sensor for these situations was proposed by J.H. Yoon *et al.* [37].

The sensing method is depicted from the desired CP combined with the targeted pH biosensing application [38]. One of the main challenges in physiological pH sensing in recent years has been monitoring the pH of wounds. The pH of wounds changes as a result of different stages of wound healing. The pH of regular skin is around 5 [39]. A low skin pH is beneficial for its function as a

barrier against bacteria and microflora. When a wound or cut occurs, the underlying tissue is exposed. This underlying tissue has a significantly higher pH to facilitate bodily functions normally protected by skin. Therefore, an initial wound occurrence leads to an increase to neutral pH, in the region of pH 7 [40]. When a wound normally heals, the pH drops to the regular healthy skin pH range where bacterial growth is inhibited (Figure 6) [41]. If the pH of a wound jumps to between 7.2-8.9 instead of decreasing, it is classified as a chronic wound [40]. Monitoring the pH of a wound gives crucial information about the healing process. Constant monitoring simplifies the identification of a chronic wound. Besides, the required treatment for chronic wounds, like applying slightly acidic pH meshes onto the wound, can be initiated in an earlier stage of the wound healing process [42].

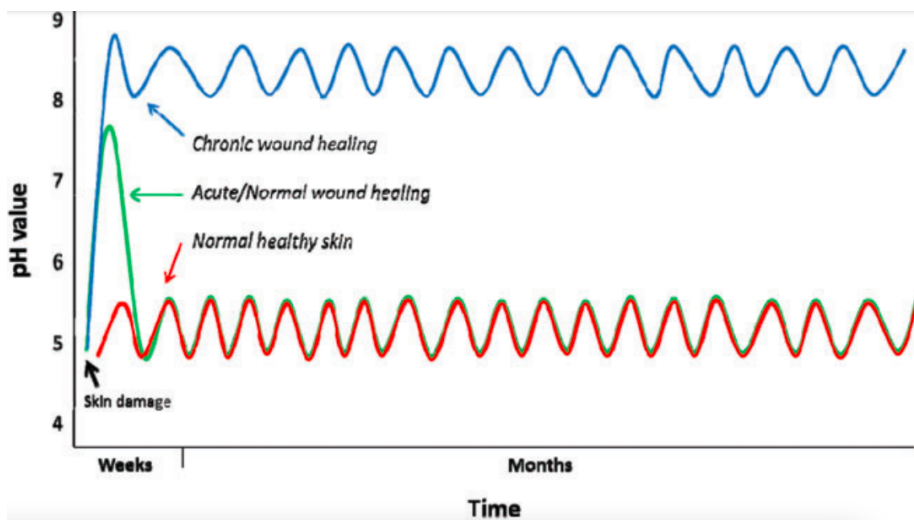


Figure 6: Propagation of the wound healing process over time with the corresponding pH response. Chronic wounds are shown to have a stable significantly higher pH. Where usual wound healing takes no longer than a month. Reproduced from E.M. Jones et al. [43].

Current pH sensing devices applied for wounds pH monitoring are not tailored for the specific use and therefore complicate real-time continuous monitoring. Because of this, wound pH monitoring is rarely done in practice for the healing of a (chronic) wound [43]. Wound pH measuring studies are mostly performed using conventional probal glass pH meters which only measure pH on the surface of one specific spot [44]. Wound dressings applied onto chronic wounds can alter the pH of wounds and benefit the speed of the wound healing process [45]. There has been a variety of studies proposing alternative pH monitoring sensor options for wound healing applications. These have been mainly focussed around metal-oxide particles incorporated in (electrospun) polymeric fiber structures. The main drawbacks posed by the use of metal-oxide nanoparticles for electrochemical sensing however are its biocompatibility concerns as well as poor long-term stability [2,3]. The poor long-term stability especially is a concern for wound fluid monitoring since sensing over longer periods of time (weeks) is required (Figure 6).

The use of CP materials for sensing can fill in the application gaps present from metal-oxide particle based sensing where CP materials are biocompatible and provide better stability in its

sensing capability [4]. Performing conductometric electrochemical sensing is a pathway to provide accurate pH measurements for CP materials. The downside of the longer detection times in conductometric sensing is irrelevant for the monitoring of pH in wound healing applications since no fast measurements are required.

For biomedical applications, the analyte materials are predominantly aqueous liquids in the pH 5-9 range [46]. For a CP to be sensitive to pH, the pKa and pKb values need to be in line with the target application pH range. pKa is defined as the acid dissociation constant of a material. pKa values are derived from the Henderson-Hasselbalch equation:

$$pH = pK_a + \log\left(\frac{[A^-]}{[HA]}\right) \quad (\text{equation 1})$$

pKb, the basic dissociation constant is derived from the pKa values. Although the actual values might differ, the theoretical definition is given as:

$$pK_b = 14 - pK_a \quad (\text{equation 2})$$

The pKa value defines the pH where a dissociation to conjugated base of 50% is achieved. The pKb is referred to as the pH value where 50% of the material is dissociated to a conjugated acid.

For sensing purposes, a constant change in signal is required in order to accurately sense a pH difference. For this reason, performing pH measurements in between the pKa and pKb values is ideal [47]. pH sensing at pKa or pKb values can greatly impact the resistance measurements and decrease the detection accuracy because of pronounced structural changes [48].

A list compiling oCVD compatible conductive polymers is constructed with the relevant properties for pH sensing (table 2). From the information in table 2, it can be seen that the option showing the highest potential to cover the full pH range for wound healing (pH 5-9) is polypyrrole. Besides, polypyrrole is seemingly biocompatible [49]. This greatly simplifies the processing requirements for real-world polypyrrole sensing applications since no surface modification is needed to include polypyrrole in a biomedical sensing device.

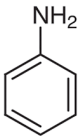
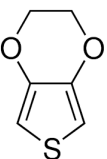
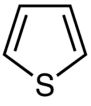
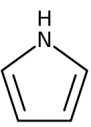
<i>Monomer</i>	<i>Structure</i>	<i>pKa</i>	<i>pKb</i>
Aniline		5.5 [50]	9.3 [51]
3,4-ethylenedioxythiophene		6.4 [52]	7.6 (equation 2)
Thiophene		3.03 [53]	8.5 [54]
Pyrrole		2-4 [48]	9-11 [55]

Table 2: Relevant  $pK_a$  and  $pK_b$  parameters essential for pH sensing of the corresponding conducting polymers. Table is limited to proven oCVD compatible monomers.

The bipolaron structure of the polypyrrole (PPy) chain (Figure 2: c) is sensitive to deprotonation which reduces the bipolaron monomer unit complexes. This process also incurs dedoping of the polymer chains, limiting the charge carrying ability of the backbone of the chain (Figure 7).

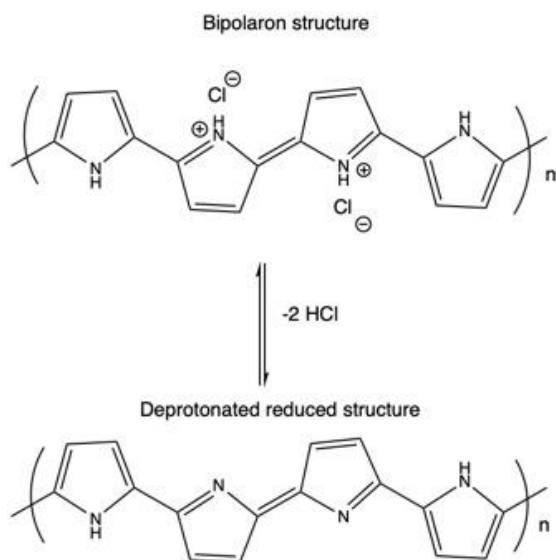


Figure 7: Deprotonation of the bipolaron polypyrrole structure to form reduced, non-conducting PPy monomer units.

The deprotonation and combined dedoping of the PPy conjugated chains leads to a structure where only neutral monomer units are present. This drastically reduces the conductivity of the PPy chains and the ability to carry the charge across the polymer system [23]. The polaron and bipolaron systems allow optical transitions between the valence and conduction bands which are not allowed in the neutral polypyrrole energy-level diagram (Figure 8) [56].

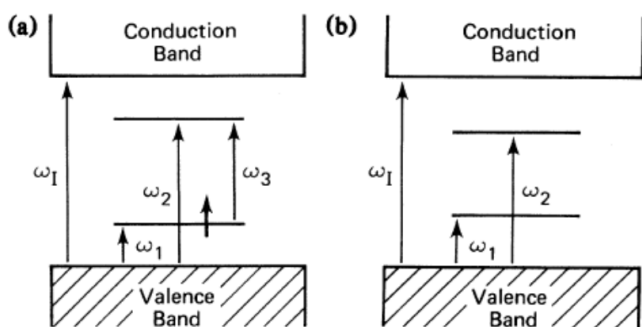


Figure 8: Allowed optical transitions for polaron states in polypyrrole (a) and bipolaron states (b). It is important to note that the polaron state has 3 allowed optical transitions where the bipolaron state has 2. This explains delocalization of bipolaron increasing conductive properties. Reproduced from J.H. Kaufman et al..

As the pKa and pKb values for polypyrrole suggest (table 2), this deprotonation reaction is dependent on the pH of the environment the PPy is subjected to. The change in conductivity that is measured on the PPy thin film is a function of the pH of the analyte that it is exposed to. The research described in this report aims to analyze the structural changes of the deprotonation of PPy as a result of exposure to different pH. Furthermore, the correlation between the deprotonation and dedoping mechanisms from pH solution exposure are analyzed. The conductometric biosensing performance of the PPy material is examined for several sensing performance parameters to display the potential of oCVD prepared PPy thin-film materials for wound fluid pH applications.

## Materials and methods

### 2.1. Materials

oCVD of PPy was performed using pyrrole, purchased from TCI Chemicals. The antimony pentachloride ( $\text{SbCl}_5$ ) oxidant for the oCVD process was purchased from Sigma Aldrich. Both reagents for oCVD were used as purchased, without further purification.

Polycarbonate sheets were used for oCVD of PPy as substrates and were acquired from Mayku, London. Poly(vinyl alcohol) (PVA,  $M_w = 31.000\text{-}50.000$  g/mol, CAS: 9002-89-5) and polyacrylonitrile (PAN,  $M_w = 150.000$  g/mol, CAS: 25014-41-9) were purchased from Sigma Aldrich. DMF solvent was acquired from Sigma Aldrich and used without any further modification as well. Silicon wafers (University Wafers Inc, Boston, USA, one side polished, 525  $\pm$  25  $\mu\text{m}$  thickness) and glass slides (Knittel Glass, 76  $\times$  26 mm dimension) were used as substrates for depositing PPy and were used for further structural analysis.

pH solutions were prepared from MilliQ water with hydrogen chloride (HCl) and sodium hydroxide (NaOH) purchased from Sigma Aldrich used with no further purification. This method leads to the presence of neutralization salts in the pH solutions. A calibrated Mettler Toledo pH meter was used to get to exact pH values for the solutions prepared.

## 2.2. Substrate independence

Recent research by S.M. Rumrill *et al.* [57] examined the differences in coating onto substrates with different wetting properties by iCVD. Differences in conformality of the deposited coating were found to be dependent on the reaction kinetics. In this research, PAN (hydrophobic) and PVA (hydrophilic) substrates were used for their significantly different surface energies. oCVD deposition of PPy is performed and subsequent deposition differences were analyzed.

### *Spin Coating*

Spin coating is used to produce solid thin films from polymer solutions. In this research, it is used to produce thin films out of PAN and PVA. PAN solution (10 wt.% in DMF) and PVA solution (15 wt.% in H<sub>2</sub>O at 80°C) were used for spin coating. Spin coating is a method to produce uniform thin films by exploiting the centrifugal force of the spinning of the substrate. The liquid solution of PAN or PVA was applied onto the center of a glass microscopic slide. The microscopic slide is rapidly spun where uniform thin films of polymer are created when the solvent evaporates from the surface. The spinning speed influences the thickness of the resulting polymer thin film after spin coating (A1). A Laurell WS-650-23B spin coater was utilized.

## 2.3. Sensing material production

The polypyrrole layer is applied onto the substrate surface by oCVD. The oCVD principle, its advantages and applications are thoroughly described in section 1.2. The solid film substrates are solid sheets of polycarbonate cut into rectangular shapes of desired sizes (A2). Using Kapton masking tape, a designated area for PPy deposition was made. This material is used for its robust mechanical properties as well as high impact and chemical resistance. Besides, it provides sufficient adhesion for the oCVD deposition of polypyrrole [58]. The nanofibrous substrate is produced by electrospinning (Figure 9).

### *Electrospinning*

Electrospinning is a production technique for the formation of nanofibers. polyacrylonitrile (PAN) is used for its hydrophobic properties which provide aqueous stability in bodily fluid pH sensing [59]. PAN is dissolved in a solvent (DMF) and continuously pumped into a needle gauge. At a distance above the needle, a collection surface is placed. A voltage is applied onto the liquid at the needle tip. The voltage charges the liquid which is the driving force for the formation of a Taylor cone. At the correct parameters for electrospinning, an undisturbed nanojet is formed (Figure 9). The charged jet is collected onto a collection surface where, due to jet whipping, these fibers are oriented in a random fashion. Several factors influence the type of nanofibers created and the corresponding jet formation. These factors include: polymer-to-solvent ratio, tip-to-collector distance, voltage applied and flow rate of the polymer solution [60]. Mean fiber diameters for produced nanofibers through electrospinning were calculated as a result of diameter analysis of 100 fibers for each sample. The parameters giving the thickest fiber diameter were taken as the appropriate electrospinning parameters to minimize the risk for oCVD to ‘crush’ the fibers. It should be noted that temperature and relative humidity generally have a significant

effect on the fiber diameter and fiber properties obtained. Day-to-day measurements may vary [61].

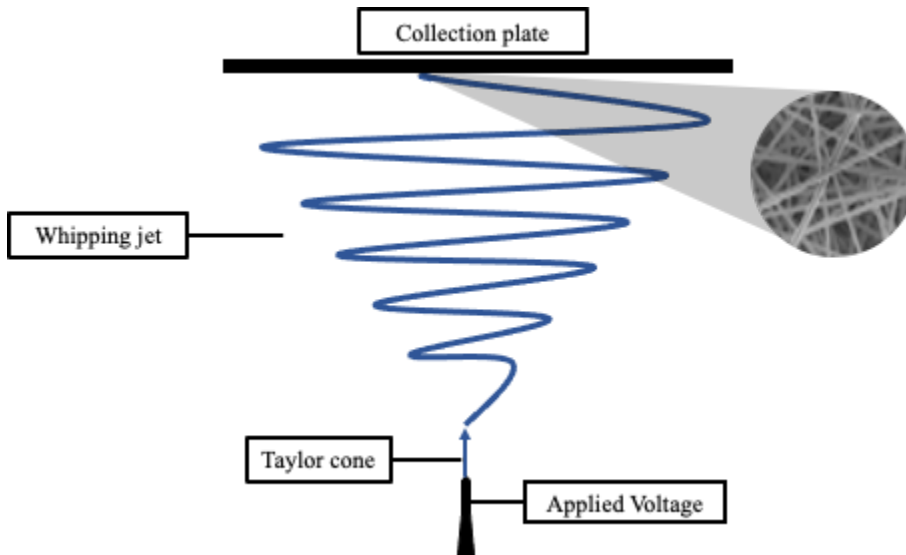


Figure 9: *Electrospinning process where a voltage is applied onto a liquid. A Taylor cone is formed followed by a jet formation. The subsequent whipping jet is collected onto a collection plate which results in formation of randomly oriented nanofibers.*

## 2.4. Structural Analysis

In this research, the structural changes in the PPy film as a result of pH solution exposure are analyzed using a variety of analytical techniques.

### *Ultraviolet-Visible Spectroscopy (UV-Vis)*

UV-Vis analysis measures the amount of light absorbed by a sample at wavelengths in the UV-Visible spectrum ranging from 300-800 nm. This research uses an Agilent Cary 60 UV-Vis Spectrophotometer. For CP's, UV-Vis analysis gives information about the optical absorption transitions and corresponding energy levels within the bandgap (Figure 8). The absorption bands positions and intensity of the spectrum allow analysis of the doping/dedoping processes in the CP sample as well as the protonation and deprotonation [62]. UV-Vis spectroscopy is based on the combination of the Beer and Faraday laws.

$$A = \frac{Q\varepsilon}{nFS} \quad (\text{Equation 3})$$

*(A being the optical absorbance, Q the charge consumed,  $\varepsilon$  the molar extinction coefficient, n the number of electrons, F the Faraday constant and S the surface area.)*

the optical absorbance is directly proportional to the charge (Equation 3).

### *Fourier-Transform Infrared Spectroscopy (FT-IR)*

IR light affects the dipole moment in molecules and subsequently its vibrational energy. Specific functional groups absorb specific wavelengths of IR radiation since all have different atoms and bond strengths. FT-IR is used to analyze these characteristic functional groups and atomic bonds [63]. With this, the characteristic PPy peaks and band areas can be located and the changes in these bands as a result of pH solution exposure can be analyzed.

IR-radiation is emitted and passed through a sample. The non-absorbed IR-radiation is detected as an interferogram and using Fourier-Transform mathematics, this is converted into absorbance as a function of the wavelength. A Shimadzu IR tracer-100 is used. Spectra were taken using a Happ-Genzel apodization taking 128 scans at a resolution of  $4\text{ cm}^{-1}$ .

### *X-ray Photoelectron Spectroscopy (XPS)*

Soft x-rays are focussed onto a solid sample. Subsequent emitted electrons as a result of these soft x-rays are analyzed by their energy. Every element has a unique spectrum of emitted electrons and can therefore be located. XPS analysis obtains a plot of detected electrons versus their kinetic energy. The environments of an element have considerable influence on the related peak shape and position. Therefore, XPS can give significant information about the chemical state of an element and the ratio [64]. This is especially useful for exact analysis of the deprotonation process described in Figure 7 which occurs as a result of pH exposure for PPy.

XPS was performed with a Surface Science SSX-100 ESCA instrument with a monochromatic Al  $K_{\alpha}$  X-ray source ( $h\nu = 1486.6\text{ eV}$ ) where the pressure in the analysis chamber was below  $5 \times 10^{-9}$  mbar. The electron take-off angle was set to  $37^{\circ}$  relative to the surface normal, and the analyzed spot had a diameter of  $1000\ \mu\text{m}$ . To prevent charging effects, a gold grid was positioned  $\approx 1\text{ mm}$  above the sample to create secondary electrons to neutralize the positive charge on the surface after photoemission. The survey spectra and detailed spectra of the  $C1s$ ,  $N1s$ ,  $Cl2p$ , and  $Sb3d$  core levels were recorded with an energy resolution of  $1.3\text{ eV}$ . The  $sp^2\ C1s$  photoemission peak of the PPy coatings at a binding energy (BE) of  $284.2\text{ eV}$  was used as the reference for the binding energies [20]. The reported binding energies have an accuracy of  $\pm 0.1\text{ eV}$ . Analysis of the XPS data was performed using the least-squares curve-fitting program, Winspec (LISE laboratory, University of Namur, Belgium), which involved subtracting a Shirley baseline and fitting with a minimum number of peaks; the peak profile was a convolution of Gaussian and Lorentzian functions. To check the uniformity of the samples, measurements were taken at two distinct spots on each sample. The uncertainty in the peak intensity determination was within 2 % for all core levels reported.

### *Scanning Electron Microscopy (SEM)*

To analyze the nanofibers produced by the electrospinning method, SEM is used. An electron beam is focussed onto a sample surface through a set of lenses. An SEM image is produced by performing backscattered electron-imaging. The material at which the electron beam is focussed absorbs part of the electrons and an amount is scattered back. The electrons that are scattered back are analyzed by a detector where different materials and atoms have different electron backscattering properties.

Besides backscattering electrons, another type of electrons are analyzed. These are called secondary electrons. Secondary electrons originate from inelastic interactions between the electron beam and sample [65]. These electrons have lower energy than the backscattering



electrons. Secondary electrons provide information about the topography and morphology of the surface of a sample at nanometer scale.

## 2.5. Sensor Performance

The sensor performance results will be conveyed using *International Union of Pure and Applied Chemistry* (IUPAC) defined definitions as much as possible. An array of components is essential for the evaluation of the performance of a PPy layer as a conductometric pH sensing device. The different performance metrics and corresponding definitions are explained in table (Table 3).

A number of experiments are required to accurately depict the pH sensing performance metrics of the sensor material. For conductometric sensing analysis both a 4-point probe sheet resistance meter (Ossila four-point probe) and 2-point probe resistance digital multimeter (DMM) was used. A 4-point probe sheet resistance meter measures the sheet resistance of a material. This technique is therefore limited to solid-film surfaces and substrates. It has four probes in a line equally spaced apart. All four probes are in contact with a film surface of the material desired to be measured. A current (I) is applied between the outer two probes with the corresponding voltage drop as a result of this current is measured on the inner two probes ( $\Delta V$ ) (Figure 10) [66].

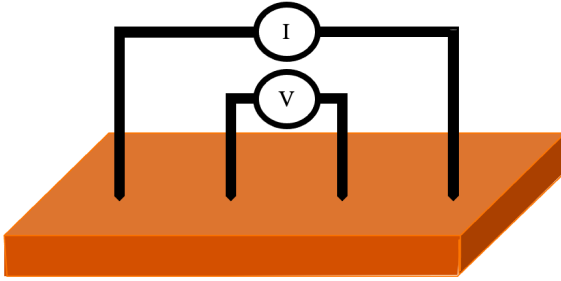


Figure 10: A 4-point probe sheet resistance meter contacting a solid film substrate. The outer two probes apply a current and the inner two probes measure a resulting voltage drop.

Sheet resistance can be calculated from the current applied and change in voltage measured.

$$R_s = 4.53236 \frac{\Delta V}{I} \quad (\text{Equation 4})$$

When the thickness of the thin-film layer is known (t), the sheet resistance ( $R_s$ ) can be used to find the conductivity.

$$C = \frac{1}{R_s \cdot t} \quad (\text{Equation 5})$$

PPy film layer thickness can be found by making use of profilometric analysis. In this study, profilometry is performed using a Bruker DEKTAK profilometer. A scratch is made on the surface of a PPy thin film such that the substrate is exposed. A sensitive needle is dragged along

the PPy film surface as well as the exposed scratch. The difference between the two depicts the deposited film layer thickness.

The sheet resistance is used for sensor analysis purposes using the change in resistance divided by the resistance of the blank to normalize the obtained result.

$$Response = \frac{R_0 - R_m}{R_0} \quad (\text{Equation 6})$$

A 4-point probe resistance meter is unsuitable for continuous time dependent measurements since it can not measure the resistance in-situ when the sensing sample is exposed to a pH solution. Time dependent continuous measurements are crucial for certain performance metrics like detection time (Table 3). In these circumstances, a 2-point probe DMM resistance meter is utilized (Figure 11). Copper wires attached to the PPy material and 2-point probe provide the possibility for continuous in-situ measurements. The resistance is always measured along the path of the least resistance [67]. Since the resistance of the PPy material is lower than the resistance of the solutions it is exposed to, this method is deemed valid (A3). Standard deviations were retrieved from the resistance measurements by performing 50 measurement repeats.

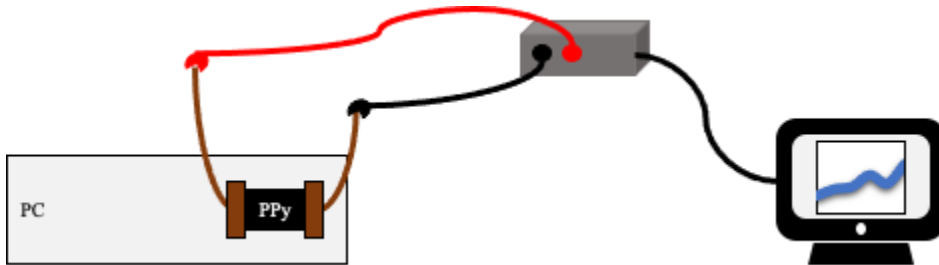


Figure 11: Set up used for continuous resistance measurements for determination of detection time, recovery time and drift (Table 3). Copper wires are attached to a sensing test strip by silver paint and further secured using copper tape. These wires are attached to a DMM device which measures the resistance of the system.

<i>Sensor performance metric</i>	<i>Measuring method</i>	<i>Unit (symbol)</i>
Limit of detection	$3 \cdot \sigma_{SD}$ (IUPAC) [68]	pH unit (LOD)

Detection time	$t_D$ : time to 90% of final signal (IUPAC) [69]	Seconds ( $t_D$ )
Recovery time	$t_R$ : time to 90% of final signal (IUPAC) [69]	Seconds ( $t_R$ )
Sensitivity	$5 \cdot \sigma_{SD}$ (FDA) [70]	pH unit (LLOQ)
Drift	$\frac{\Delta R_{R_0}}{\Delta t}$ (IUPAC) [71]	$\frac{\Omega}{min}$ (drift)

Table 3: Key pH sensor performance metrics, corresponding measurement definitions and units related to the performance metric defined.

## 2.6. Research Aim

This research aims to analyze the substrate independence of oCVD by varying the surface energy of substrates, namely: PAN (hydrophobic, high in energy) and PVA (hydrophilic, low in energy). Both PAN and PVA substrates were produced by spin coating onto a glass microscopic slide. Using profilometry (section 2.5), the thickness of these substrates before and after oCVD deposition of PPy was examined. The oCVD deposition of PPy was done in the same reaction run to analyze the differences. Switching the position of the substrate inside the reaction chamber is done to remove the influence of the reaction chamber position dependency of the deposition rate. Because oCVD is deemed to be a plug-flow type reaction process, the thickness of the PPy deposition is dependent on the position of the substrate in the reaction chamber [72].

The performance of the electrical resistance response of PPy due to pH induced stimuli is aimed to be characterized according to a set of performance metrics. PPy shows great potential to be used in (bio)sensing devices due to its ideal pH sensitive range for physiological pH sensing. The potential for improved processability oCVD PPy to be implemented into sensor devices is aimed to be displayed from the performance metrics and put into context regarding other state-of-the-art pH sensing devices.

PPy structural changes as a result of pH induced stimuli result in a changing electrical conductivity observed by the electrical resistance changes. The exact structural changes are aimed to be analyzed using a variety of analytical methods. The contribution of different units in the PPy structure and the structural changes occurring are aimed to be correlated with the electrical resistance changes.

## Results and Discussion

### 3.1. oCVD substrate independence

The substrate dependence of the oCVD of PPy was investigated by the deposition rate of PPy on substrates with varying surface energies. Figure 12 shows the deposition rate of oCVD PPy on a hydrophilic PVA surface and a hydrophobic PAN substrate. The results indicate that the oCVD of PPy does not occur preferentially on a surface with different surface energies, thus, suggesting the substrate independence of the vapor phase processing. Standard deviations are relatively large which could be attributed to two effects:

- Spin coating conformality is imperfect which results in a thickness error before oCVD.
- oCVD is deemed to be a plug-flow reaction process, the thickness of the PPy deposition is dependent on the positions of the substrate in the reaction chamber.

Previous research by Rumrill *et. al.* [57] reported similar observations attesting to the substrate independence of iCVD - a closely analogous vapor phase processing technique as oCVD, supporting our analysis.

The proof that there is no dependence of substrate on the thickness of the PPy deposition obtained helps with analyzing the thickness and subsequent conductivity of the sensing materials produced (Equation 5). The thickness of the PPy layer is only dependent on the oCVD reaction parameters.

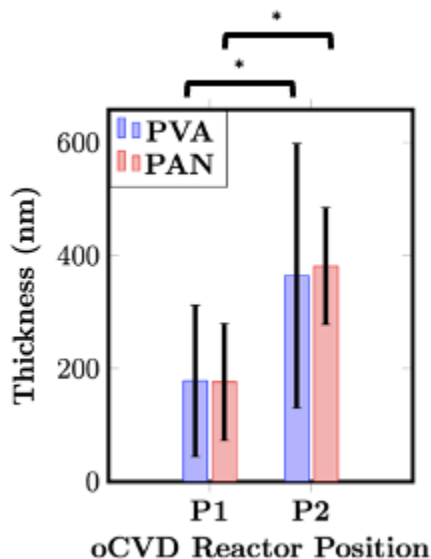


Figure 12: Influence of surface energies of the substrates on oCVD deposition rate and subsequent oCVD thickness. P1 and P2 are two different places inside the reaction chamber where the substrates were placed.

### 3.2. UV-Vis Analysis

oCVD deposited thin-films on quartz substrates were used for UV-Vis analysis. UV-Vis gives information about the optical band gap transitions. The protonation/ deprotonation of the PPy thin film as well as the dopant concentration can be deduced from the position of these bands as well as the absorbance intensity observed. The long-term effect of the exposure of a (type 2 oCVD produced) PPy thin film to an aqueous solution was analyzed by UV-Vis (Figure 13). Two broad absorption bands can be observed in the spectrum. The  $\pi-\pi^*$  - transition between the valence and conduction bands can be observed at 350-550 nm wavelengths. This transition corresponds to a transition which is only present in the polaron and bipolaron states of the PPy (Figure 8) [73]. The broad band at higher wavelengths (600-800 nm) can be allocated to the presence of bipolarons where it is the transition from the valence band to the closest bipolaron transition state [74]. Bipolarons are produced in-situ in the oCVD process which can be seen from the non-exposed PPy thin-film having a strong absorption band in the 600-800 nm region. Bipolarons are produced in-situ through the oCVD process including  $\text{Cl}^-$  dopant anion. Because of this, there is a direct correlation between the dopant concentration and the bipolarons present in the PPy chain. Therefore, the doping concentration in the PPy chains can be correlated to the intensity of the bipolaron optical transition band visible in the UV-Vis spectrum [75].

It should be noted that a red-shift transition in the peak of the  $\pi-\pi^*$  - transition band shifts to lower wavelengths with increasing aqueous solution exposure time (purple line, Figure 13). This is attributed to the decrease in conjugation length with increasing exposure time. The decrease in absorption intensity reflects the decrease in  $\pi-\pi^*$  - transition activity. The 600-800 nm transition band allocated to the bipolarons present in the PPy chains shows a clear trend where the absorbance intensity decreases with increasing aqueous exposure time. The results indicate that the concentration as well as the amount of bipolarons in the PPy chains is decreasing with increasing aqueous solution exposure time [76]. The decrease in the concentration of bipolarons decreases the conductivity of the PPy thin film and is a result of the deprotonation of the polypyrrole chains due to aqueous exposure (Figure 7) [77].

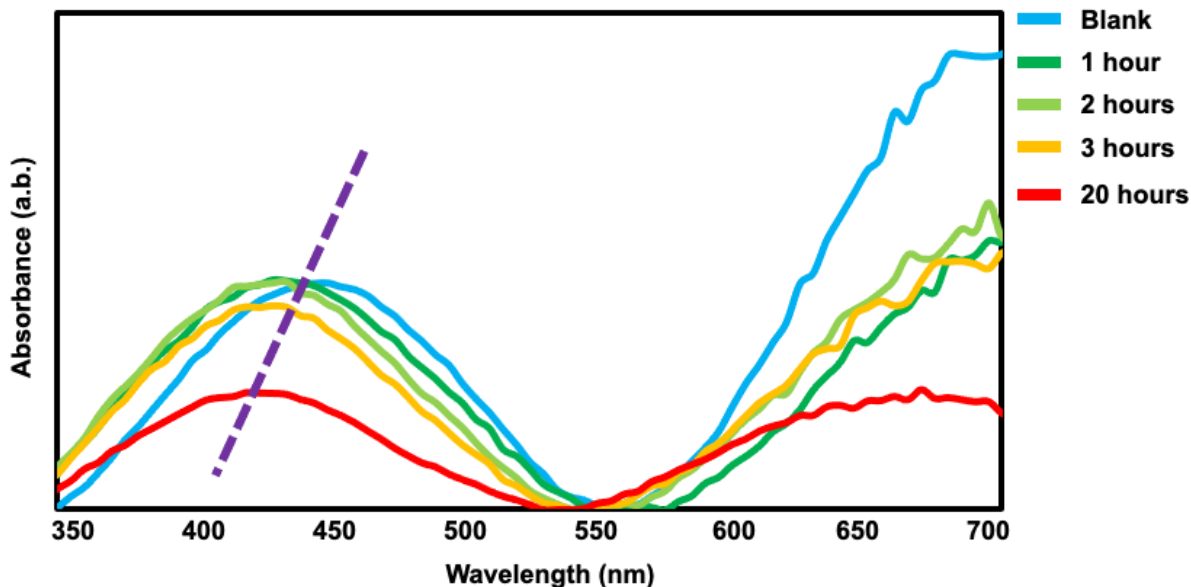


Figure 13: *UV-Vis spectrum of oCVD PPy exposed to an aqueous (pH 7) solution. Spectra taken at time points of 0, 1, 2, 3, and 20 hours. Purple line showing the red-shift in the position of the  $\pi-\pi^*$  - transition band with increasing time.*

Besides the long-term exposure of oCVD PPy to neutral pH, the effect of different pH solutions on the optical transition bands observed by UV-Vis spectroscopic analysis was examined (Figure 14). The results show again the characteristic PPy optical transition bands at 350-550 nm in addition to the bipolaron 600-800 transition. A drastic decrease in absorbance intensity of both the characteristic bands with increasing pH can be observed. Similar to the results from Figure 13 for oCVD PPy, a red-shift is observed when exposing oCVD PPy to increasing pH: The  $\pi-\pi^*$  - transition band position shifts to lower wavelength.

The drastic decrease in absorbance at both the 350-550  $\pi-\pi^*$  - transition as well as the 600-800 nm bipolaron transition can be explained by the pKa and pKb of PPy and the corresponding deprotonation (Table 2). A minor recovery in absorbance intensity in both the  $\pi-\pi^*$  - transition band as well as the bipolaron band is observed when, after stepwise exposure to pH 5-9, the PPy thin film is exposed to pH 5 again (purple spectrum, Figure 14). This recovery showcases the reversibility of the deprotonation corresponding to the bipolaron units in the PPy chains.

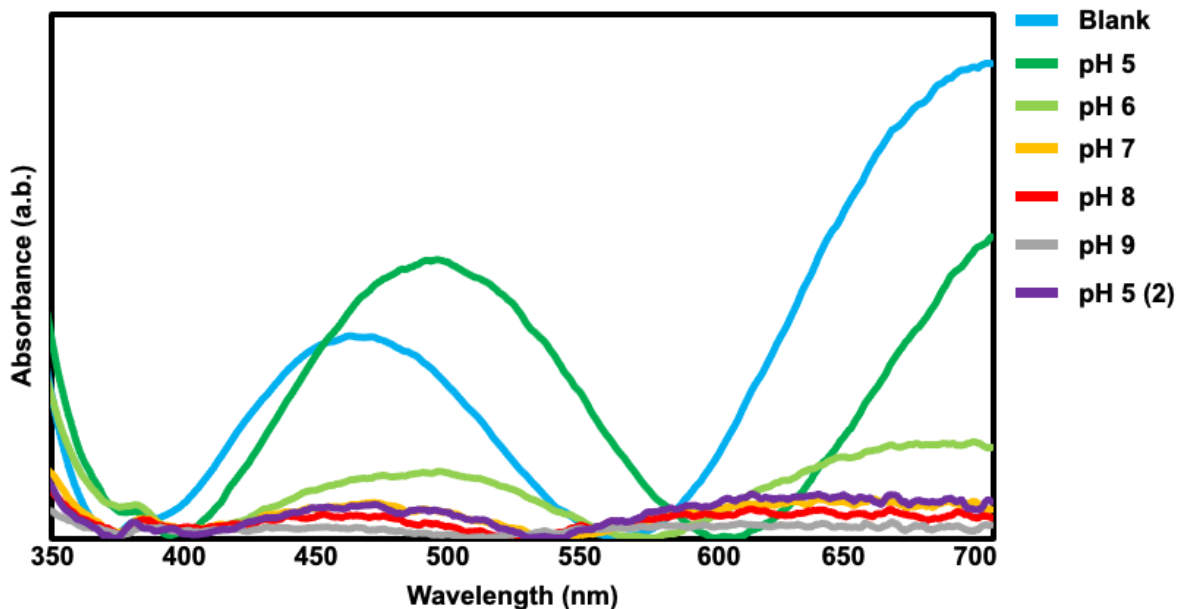


Figure 14: *oCVD PPy* exposed to different pH solutions for equal times (15 minutes). pH 5 (2) being exposure to pH 5 after it has been exposed to all previous solutions.

The band gap energies corresponding to the PPy thin-film exposed to different pH were found from Tauc plots constructed from UV-Vis data from Figure 14 (A11). The band gap energies for the PPy thin-film are shown in Table 4. An increase in the optical band gap energy is observed for increasing pH exposure. This trend is in agreement with the observed increase in electrical resistance with increasing pH.

<i>Type of exposure</i>	<i>Band gap energy</i>
Blank (control)	3.5 eV
pH 5	3.5 eV
pH 6	3.6 eV
pH 7	3.7 eV
pH 8	3.7 eV
pH 9	3.7 eV
pH 5 (2nd)	3.7 eV

Table 4: *Band gap energies at different pH exposures of oCVD PPy found from a linear fit of the Tauc plots constructed from the UV-Vis data in Figure 14 (A11).*

### 3.3. FT-IR Analysis

Ultra-thin coatings of PPy were deposited via oCVD. Figure 15 shows the FT-IR spectrum of pristine, as deposited PPy. Figure 15 shows the FT-IR spectrum of an as-deposited oCVD PPy thin-film on an IR-transparent silicon wafer. The band allocated for the absorption spectrum in Figure 15 can be found in Table 5 [23,78,79].

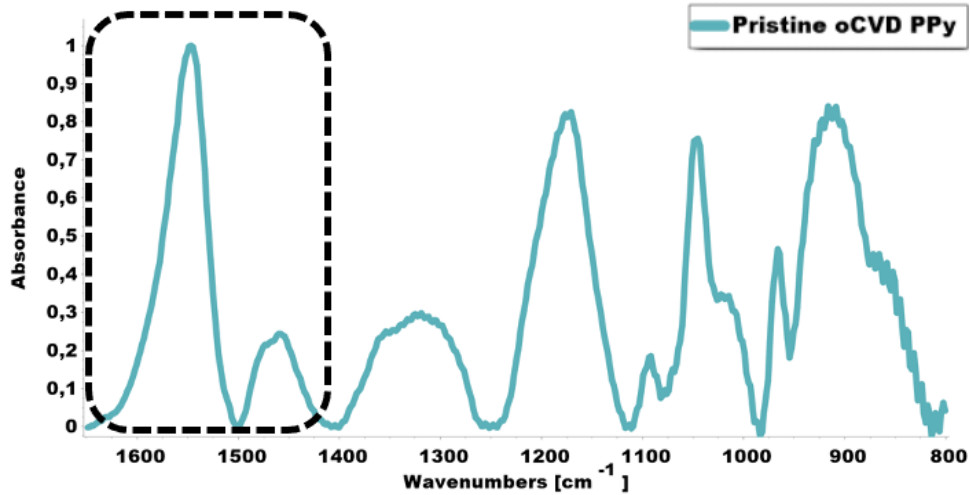


Figure 15: Graphical representation of the full FT-IR spectrum of pristine PPy. The analysis of deprotonation will focus on the  $1550\text{ cm}^{-1}$  (C=C/C-C) absorption band and the  $1475\text{ cm}^{-1}$  (C-N/C-C) absorption.

<i>Band Position (cm<sup>-1</sup>)</i>	<i>Assignment</i>
1550*	C=C/C-C
1475*	C-N/C-C
1295	C-H bending (in-plane)
1168	Ring breathing
1093	N-H <sup>+</sup> deformation
1040	C-H bending (in-plane)
965	Cl <sup>-</sup> dopant
915	C-H bending

Table 5: FT-IR peak assignment corresponding to pristine as deposited oCVD PPy. absorption bands marked with (\*) shows the characteristic bands corresponding to PPy.

A blue-shift is observed for almost all peaks with increasing pH (A12). This is due to the shortening of the conjugation length resulting from increasing pH solution exposure. Shortening of conjugation length of the PPy chains impacts the electrical resistance of the thin-film [80]. The absorbance intensity of the  $965\text{ cm}^{-1}$  chloride dopant peak decreases with increasing pH it is exposed to. This suggests a dedoping of bipolaron units in the PPy chain. Dedoping and

deprotonation are directly correlated which indicates a corresponding deprotonation [75]. This is in line with the observed increase in electrical resistance of the PPy thin-film with increasing pH.

A splitting of the C=C/C-C absorption band is observed in the PPy FT-IR spectrum when exposed to pH solutions (Figure 16). Previous literature reports have not observed or described this absorption band splitting phenomenon, the distinguishing of the peak rarely transpires [81–84]. It is suggested the observed peak splitting is the influence of the polaron and bipolaron contributions to the FT-IR spectrum. Bipolarons and polarons have different relative conjugation lengths due to the differences in the ability to hop across the PPy chains [85]. Bipolaron conjugation length is limited to four monomer units where polarons can extend over up to 50 pyrrole monomer units [10,86]. The bipolaron absorption can be positioned at higher wavenumbers due to the shorter conjugation length [87]. This effect is visible in Figure 16 where the polaron contribution to the C=C/C-C absorption band is found at  $1530\text{ cm}^{-1}$ . The splitting of the C=C/C-C absorption band due to bipolaron and polaron contributions is extremely severe. The severity of this phenomenon indicates that distinctive properties related to the production method (oCVD) of PPy have an effect. oCVD produced PPy has a significantly higher conjugation length of the polymer chains [20]. Besides, the doping concentration, and consequently the bipolaron and polaron concentration in the chains is relatively high. This results in a high amount of polarons being able to extend over more pyrrole monomer units. As the PPy chains are deprotonated, the relative intensity of the  $1550\text{ cm}^{-1}$  (bipolaron) absorption band decreases making the relative contribution of the polaron absorption more pronounced.

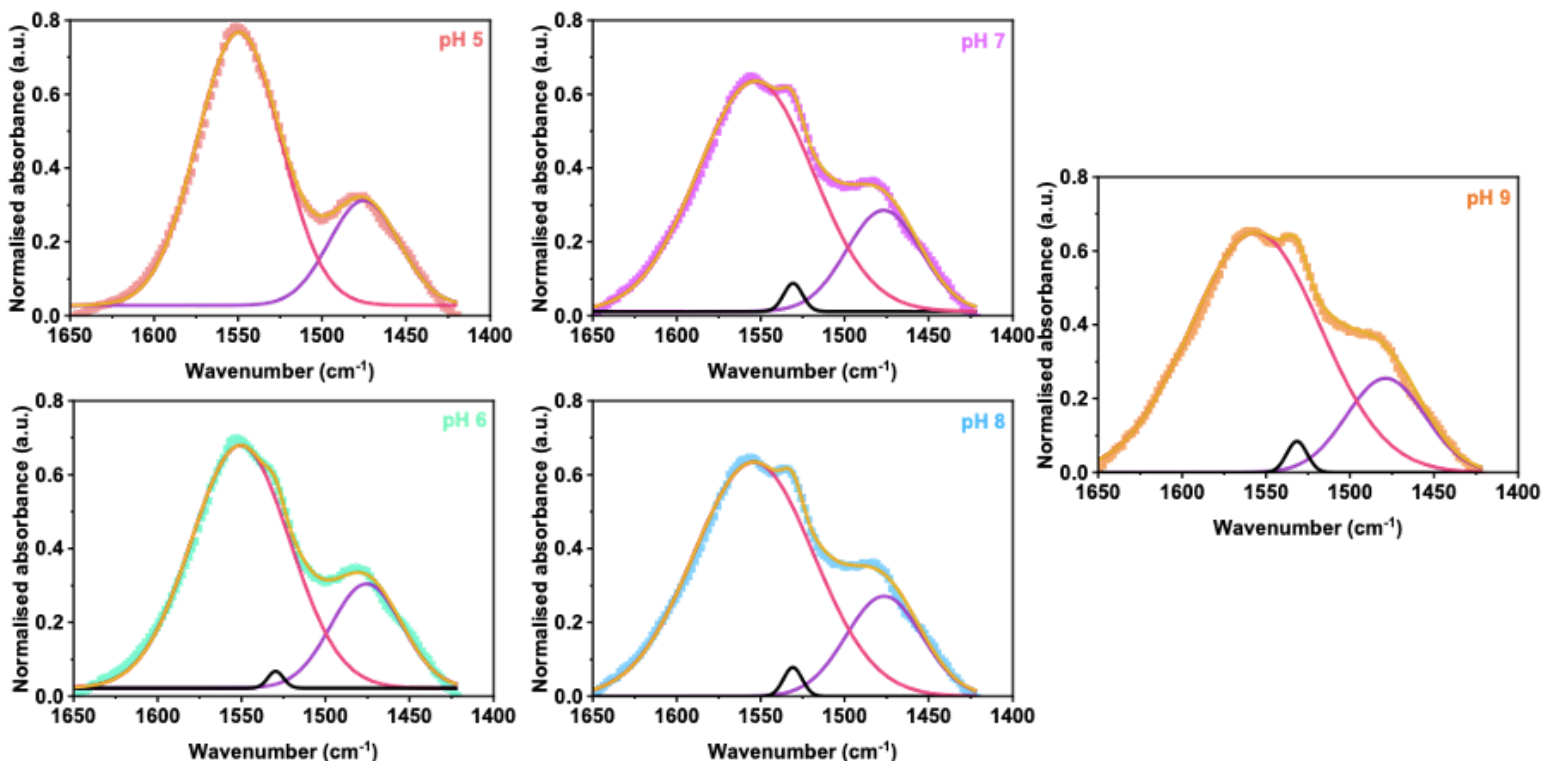


Figure 16: Peak deconvolution of the FT-IR spectrum of oCVD PPy subjected to pH 5, 6, 7, 8 and 9.  $1550\text{ cm}^{-1}$  and  $1475\text{ cm}^{-1}$  absorption bands corresponding to the C=C/C-C and C-N/C-C absorption bands. PPy The appearance of a new polaron related band at  $1530\text{ cm}^{-1}$  becomes more apparent at higher pH.



A correlation between the conductivity and the ratio between the intensity of the C=C/C-C (1550  $\text{cm}^{-1}$ ) and C-N/C-C (1475  $\text{cm}^{-1}$ ) absorption bands has been proposed by Tian and Zerbi [88]. The resistance increase is proportional to the ratio of the intensity of the two absorption bands, the effective conjugation coordinate (ECC) [89]. Since the conjugation length is related to the conductivity, the ECC can be inversely correlated to the conjugation length of the PPy chains. This concept has been widely used in other works on PPy [90].

$$ECC = (A_{1550 \text{ cm}^{-1}}/A_{1475 \text{ cm}^{-1}}) \quad (\text{Equation 7})$$

Figure 17 shows the increase in the effective conjugation coordinate (black) with increasing pH solution exposure in line with the increase in resistance trend found in Figure 25. The observation of the polaron absorption band at 1530  $\text{cm}^{-1}$  follows a trend where the relative ratio between the bipolaron and polaron absorption is proportional to the electrical resistance as well. This phenomenon is examined by a parameter newly defined as effective polaron contribution (EPC).

$$EPC = A_{1530 \text{ cm}^{-1}}/(A_{1550 \text{ cm}^{-1}} + A_{1530 \text{ cm}^{-1}}) (\cdot 100\%) \quad (\text{Equation 8})$$

The increase in EPC as a function of the pH the PPy thin-film is exposed to is visualized in Figure 17 (red).

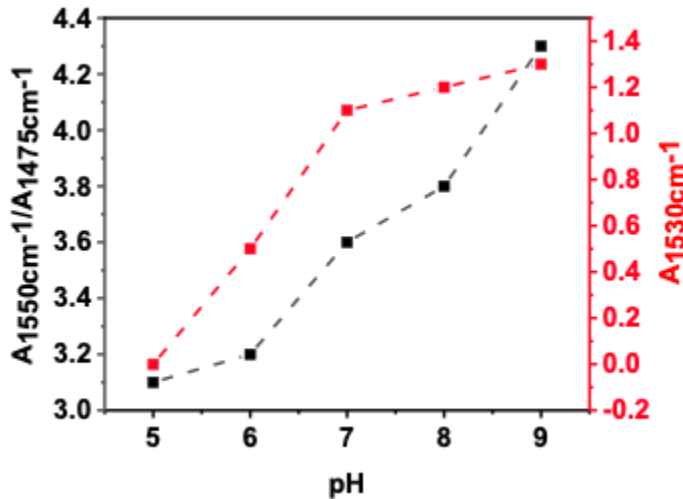


Figure 17: Increase of the ECC (Equation 7) as a function of pH exposure (black). Increase of the EPC as a function of pH exposure is visualized in red (Equation 8).

### 3.4. XPS Analysis

PPy thin-films were produced through oCVD using type 2 PPy production parameters on glass substrates. A pristine (non-exposed) PPy thin-film e was used as a control where samples exposed

to different pH solutions (5, 8 and 11) were analyzed for deprotonation. Figure 18 shows the survey spectra where the control shows the presence of all characteristic PPy constituent elements (C, N and Cl-dopant) as well as the residual oxidant used for oCVD production in the form of antimony. A small presence of O was detected which originates from overoxidation of the PPy rings during the oxidative polymerization process [20]. No observation of the Si element was seen suggesting that the PPy thin-film was conformally deposited onto the glass substrate. After exposure to pH solution, the presence of antimony in the system decreased significantly (Figure 18).

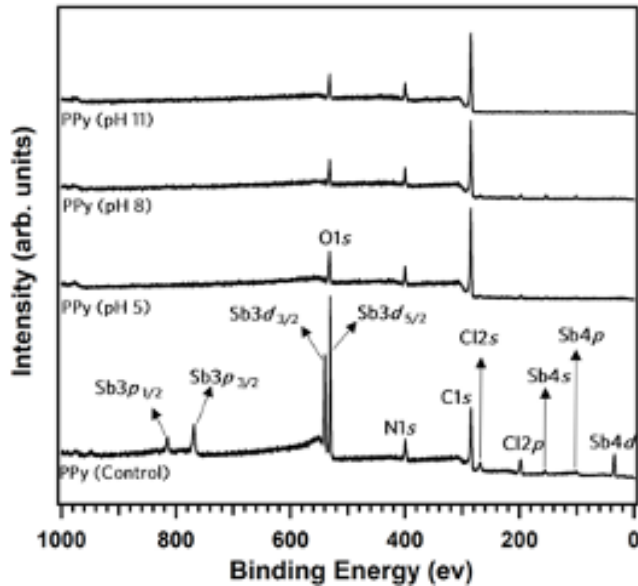


Figure 18: XPS survey spectra for oCVD deposited PPy thin-film on glass substrates. Spectra shown as deposited (bottom) and exposed to pH 5, 8 and 11. Produced by H. Hemmatpour.

The stoichiometric analysis involved collecting detailed core level spectra of C1s, N1s, O1s, Sb3d, and Cl2p for all samples. The corresponding atomic percentages in the probed volume is presented in Table 1. The atomic percentages of Sb and Cl exhibited a significant decrease with exposure to pH. The atomic percentage of Sb, decreased from 8.8 at.% in the pristine sample to 0.1-0.3 at.% with the pH exposed samples. This decline indicates that the impurities from the doping agent (SbCl5) present at the pristine PPy sample from the oCVD PPy deposition process are washed off in pH solution. Besides, the atomic percentage of Cl decreases from 7.1 at.% in the pristine sample to 0.2-1.8 at.% in pH exposed samples. This indicates a deprotonation process where dopant anions are correlated to the deprotonation of the PPy chains [75,91].

<i>PPy samples</i>	<i>Atomic percentage (<math>\pm 2</math> at. %)</i>				
	<b>C</b>	<b>N</b>	<b>O</b>	<b>Sb</b>	<b>Cl</b>
Pristine	64.6	12.7	6.8	8.8	7.1
pH 5	77.6	8.8	12.3	0.2	1.0
pH 8	76.7	11.1	10.1	0.3	1.8
pH 11	79.1	10.7	9.9	0.1	0.2

Table 6: Chemical composition on the surface of oCVD deposited PPy thin-films on glass substrates. Table showing the pristine PPy sample as well as PPy exposed to pH 5, 8 and 11.

The detailed XPS spectra of the N1s core level region of PPy exposed to different pH can be found in Figure 19. All spectra exhibit an asymmetrical peak where four components are used for a fit. The main peak located at a binding energy (BE) of 399.7 eV (red, Figure 19) is attributed to the -NH- species in the pyrrole ring (Figure 2) [20]. The other components at a BE of 397.7 eV (green), 401.2 eV (blue) and 402.6 eV (cyan) result from C=N, C-N<sup>+</sup>, and C=N<sup>+</sup> nitrogen species. From Figure 19, it can be seen that as the pH the PPy is exposed to increases, the contribution of the peak associated with C=N nitrogen species becomes more pronounced. The intensity of the components attributed to positively charged nitrogen decreases. When combined, the relative percentage of the positively charged nitrogen species (C-N<sup>+</sup> and C=N<sup>+</sup>) decrease from 23.7 % to 18 %. The relative percentage of C=N species increases from 8.8 % to 19.4 % with increasing pH exposure from 5 to 11. This suggests that the oCVD produced PPy thin-films charge concentration decreases when exposed to increasing pH. This observed structural change is in line with the pKa and pKb values for PPy where a deprotonation effect is expected which becomes more severe with increasing pH (Figure 7). The N1s XPS results indicate that the nitrogen species undergo deprotonation at increasing pH exposure.

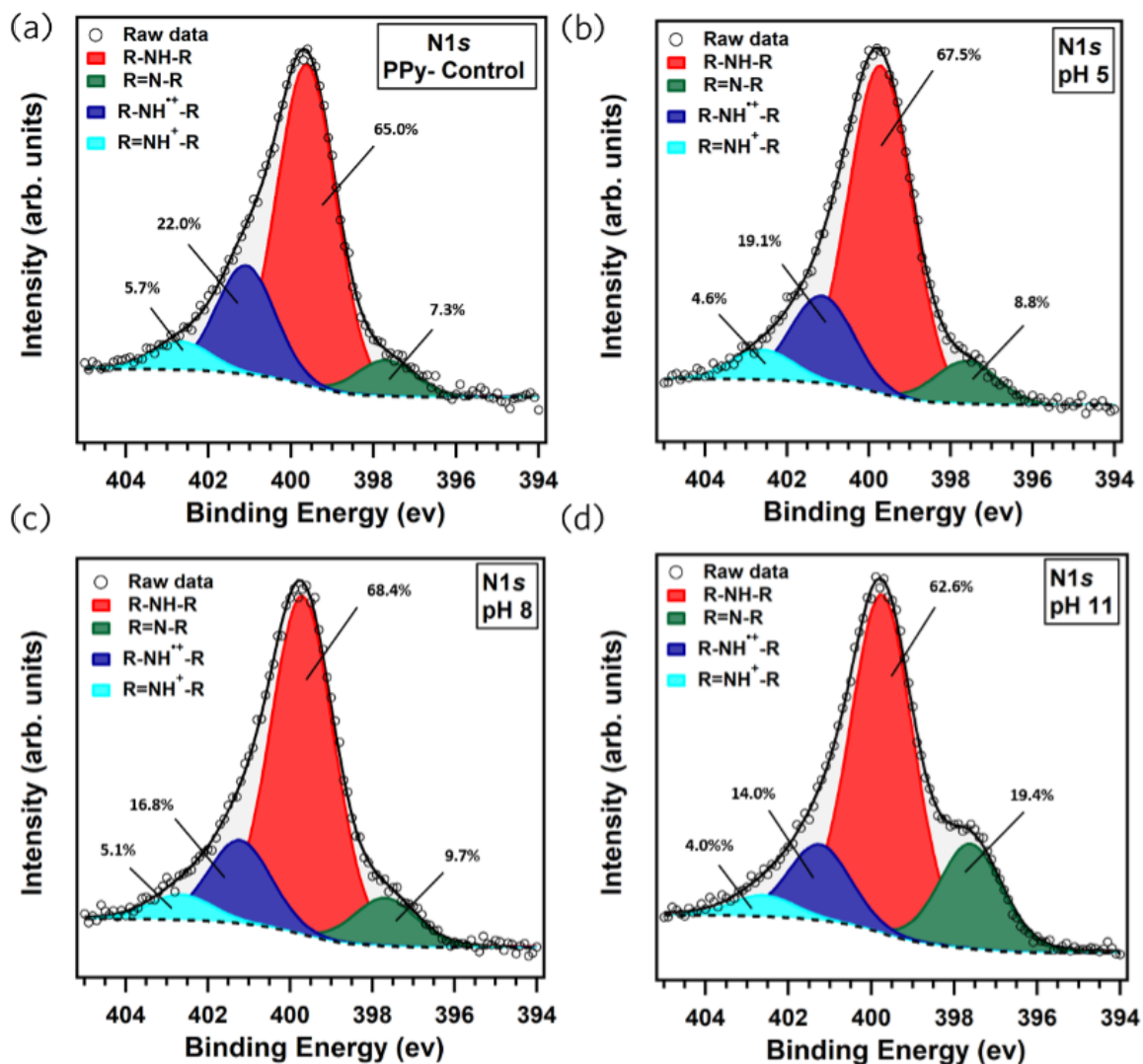


Figure 19: XPS spectra of the N1s core level region of oCVD deposited PPy thin-films on glass substrates after exposure to pH 5, 8 and 11. Produced by H. Hemmatpour.

The C1s core level XPS spectra of the oCVD produced PPy thin films shown in Figure 20 shows the presence of at least five distinct chemical species. The major contribution to the C1s line, identified at a BE of 284.2 eV (purple), is assigned to  $sp^2$  C=C species [20]. Besides, three other components at BEs of 285.1 eV (red), 286.1 eV (green) and 287.3 eV (cyan) are designated to C-N (pyrrole N), C-O/C-N<sup>+</sup>/C=N, and C=O/C=N<sup>+</sup> carbon species [92]. Another peak observed at a BE of 289.2 eV (orange) can be assigned to a shake-up [92]. When the PPy thin films on glass substrates are exposed to pH 5 to 11, the relative intensity of the C-N component increases from 27.0 % to 31.0 %. This change is consistent with the interpretation of N1s core level spectra where more neutral PPy chains are expected to form due to deprotonation when it is exposed to increasing pH (Figure 7).

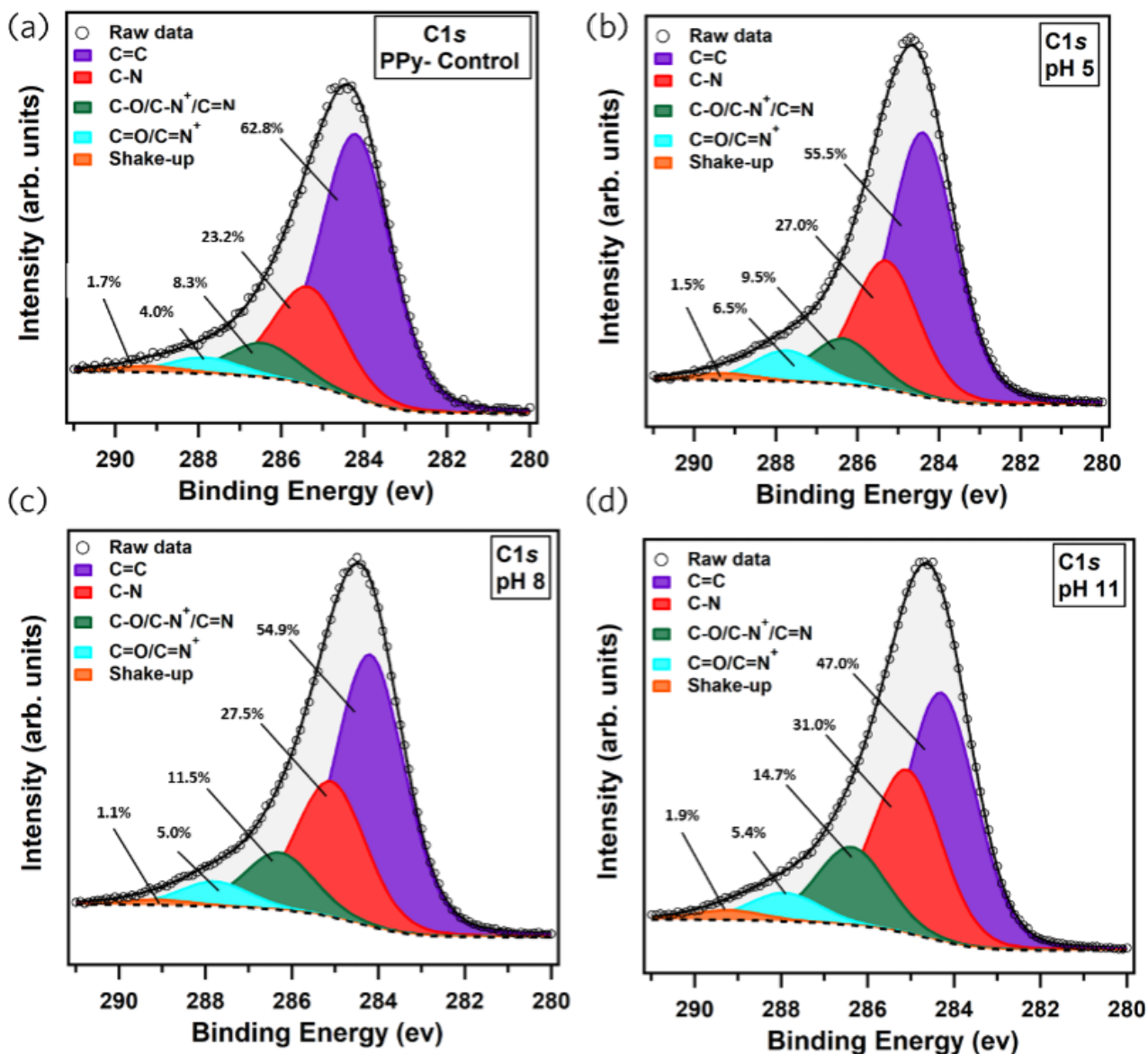


Figure 20: XPS spectra of the C1s core level region of oCVD deposited PPy thin films after exposure to pH 5, 8 and 11. Produced by H. Hemmatpour.

The Cl2p core level spectra for the oCVD deposited PPy thin films on a glass substrate can be seen in Figure 21. As shown in Figure 21 (a), the pristine PPy control sample, the spectrum requires three components for a satisfactory fit; the one at a BE of 197.4 eV (olive green) is assigned to the Cl anion, the component peaked at a BE of 198.4 eV (green) corresponds to Cl-N<sup>+</sup> and the signal at a BE of 199.9 eV (pink) is assigned to the covalent Cl-carbon (C-Cl) bond [20]. The Cl-N<sup>+</sup> species acts as an intermediary in the charge transfer process between the PPy backbone and chloride anions, and has a significant impact on the conductivity of the PPy thin-film [93]. Subsequently, with increasing pH exposure, it can be seen that the intensity of the part assigned to this component significantly diminishes. This is due to the deprotonation process which results in the loss of HCl molecules from the PPy chains and falls in line with the observed increase in resistance response with increasing pH (Figure 25). Additionally, a decrease in the atomic percentage of Cl anions present is observed with increasing pH. After exposure to a pH 11

solution, the chlorine in the sample is primarily forming of C-Cl bonds, suggesting that the charge of the PPy thin film is compensated through the deprotonation process.

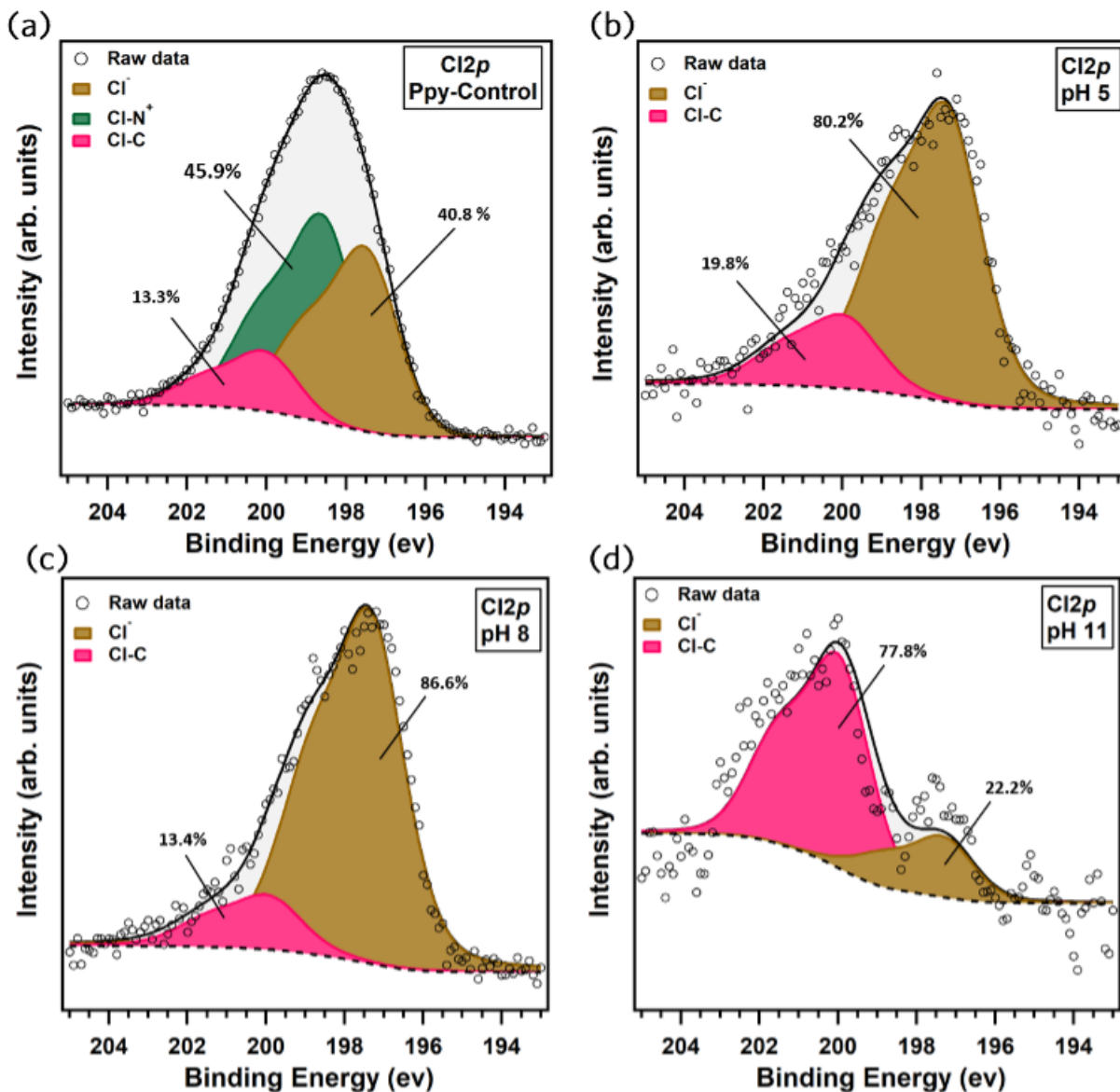


Figure 21: XPS spectra of the Cl2p core level region of PPy coatings after exposure to pH 5, 8 and 11. Graph produced by H. Hemmatpour.

### 3.5. Sensing Material Performance

#### *Sensing Material Construction*

To analyze the optimal chemical composition of PPy thin-film layer for pH sensing, two types of PPy were oCVD deposited where the bipolaron and dopant concentration was changed. This was done by changing the so-called ‘reactant ratio’ for the PPy deposition. The reactant ratio (RR) is the ratio of the flow rate between the monomer and oxidant. The RR influences the doping and

bipolaron concentration of the PPy chains [20]. The parameters used for oCVD reactions to deposit the conducting PPy layer onto the substrate are summarized Table 7. The divergent concentrations of bipolarons and corresponding doping in the PPy layer allows for a change in the amount of deprotonation sites present in the PPy chains (Figure 22). These differences have a significant effect on the electrical resistance response of the PPy film as a result of pH induced stimuli.

<i>oCVD reaction parameters</i>	<i>Type 1 PPy</i>	<i>Type 2 PPy</i>
<i>Reaction temperature</i>	40 °C	40 °C
<i>Pyrrole monomer flow rate</i>	2.50 sccm	2.50 sccm
<i>SbCl<sub>5</sub> oxidant flow rate</i>	0.25 sccm	0.50 sccm
<i>N<sub>2</sub> patch-flow rate</i>	10 sccm	10 sccm
<i>Deposition pressure</i>	300 mTorr	300 mTorr
<i>Deposition time</i>	60 min	60 min

Table 7: oCVD parameters used for the deposition of two different types of PPy onto a polycarbonate substrate for the pH sensing. Pyrrole and SbCl<sub>5</sub> flow rates are altered.

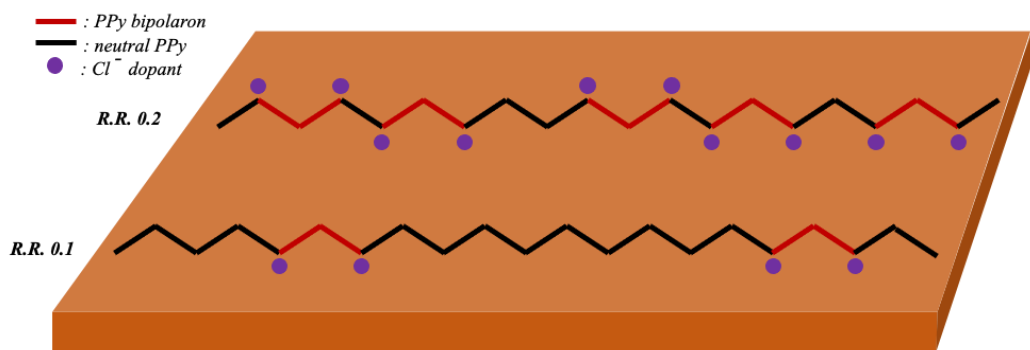


Figure 22: Schematic representation of the differences in deposition of type 1 (R.R. 0.1) and type 2 (R.R. 0.2) PPy. Type 1 is deemed having a lower amount of bipolarons and doping in the PPy chains compared to type 2 PPy.

In an effort to combine both miniaturizability with increased surface area for improved sensor performance, Bhattacharyya *et al.* have exploited the ability of oCVD polymerization to deposit through the bulk and constructed PEDOT deposited porous nylon nanofiber complexes. These 3D complexes significantly increase the surface-to-volume ratio of the active sensing layer [94].

Figure 23 shows PAN nanofibers produced using an electrospinning process described in section 2.3. A survey using a variety of parameters was carried out in order to achieve beading-free fibers of thicknesses appropriate for oCVD (A4) [95].



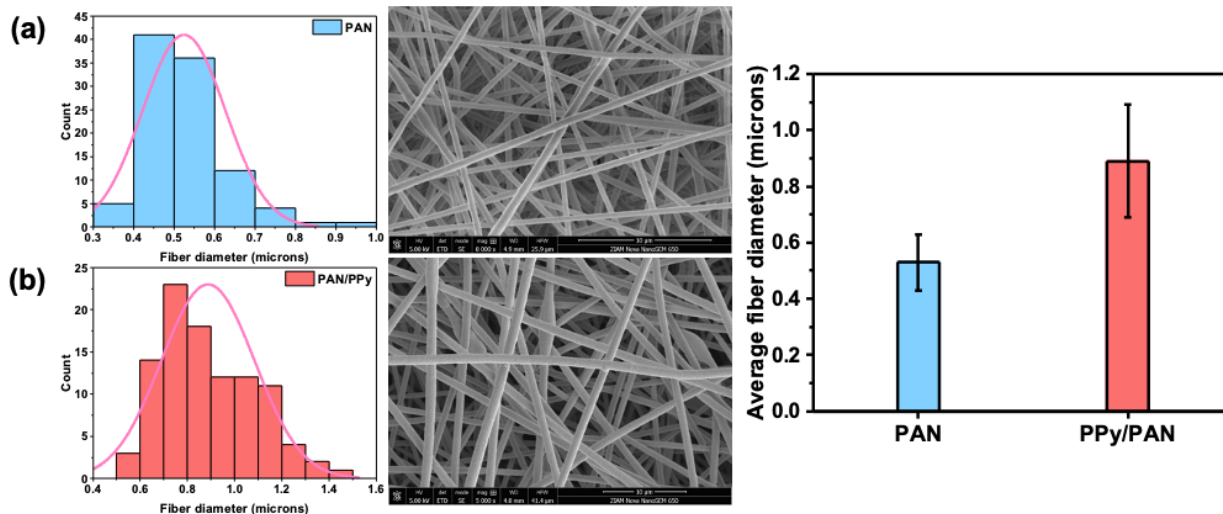


Figure 23: Fiber diameter and morphology analysis of (a) uncoated polyacrylonitrile (PAN) nanofibers, (b) oCVD PPy/PAN fiber mats showing a clear increase in fiber diameter after oCVD.

From the data represented in Figure 23, it is observed that the fibers grew in diameter size suggesting successful oCVD of PPy (A5). Figure 24 shows the stacked FT-IR spectra of PAN, PAN/PPy fibers and the oCVD PPy spectrum. Arrows are pointed at the characteristic absorption bands present in the PAN (yellow) and PPy (blue) spectra. All characteristic peaks of both PAN and PPy are present in the PAN/PPy spectrum (red).

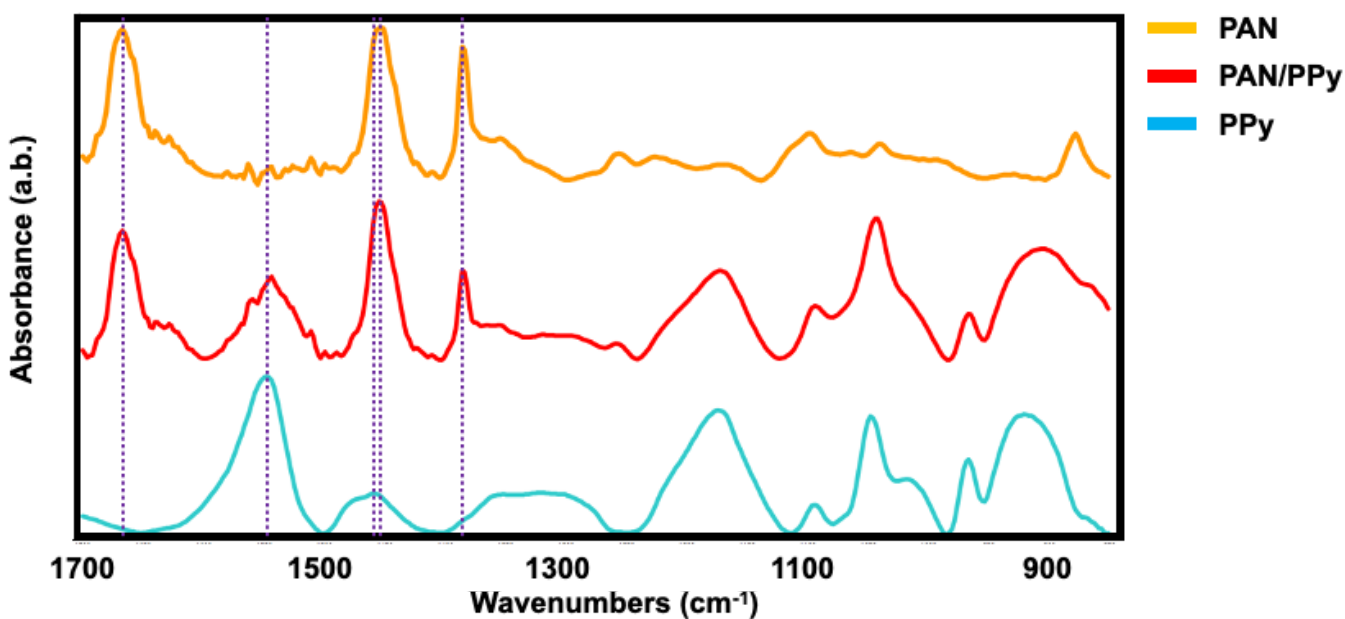




Figure 24: Comparison of the FT-IR of pure PAN (yellow), PAN/PPy nanofibers produced by electrospinning and oCVD (red) and oCVD PPy (blue). Characteristic peaks of PAN and PPy can be seen by purple lines.

### Electrical Resistance Response

The performance of the three PPy thin-film pH sensing materials was measured according to the performance metrics in Table 3. The electrospun complex is not suitable for 4-point probe sheet resistance measurements due to it having a surface area through the bulk. Therefore, all performance metrics were calculated from DMM measurements.

The electrical resistance response curves (Equation 6) of all three sensing material types are compared in Figure 25. Resistance data points were found for pH 5-9. A second-order polynomial fit to the experimental data (Figure 25) shows the electrical resistance response increases with pH (A6). This is expected due to the proposed deprotonation of the PPy chains at basic pH according to the dissociation constants (Table 2). Deprotonation is correlated to an electrical resistance increase [23].

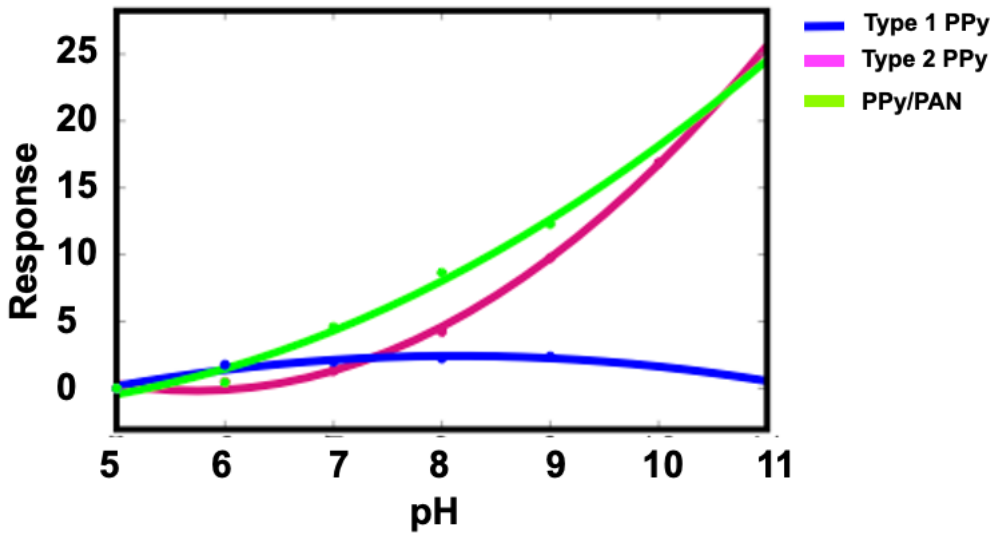


Figure 25: Comparison of the three types of PPy pH sensing materials produced. Electrical resistance response vs. pH. RR 0.1 PPy (blue) RR 0.2 PPy (magenta) and fiber constructed PPy/PAN (green).

Limit of detection (LOD) and sensitivity (lower limit of quantification, LLOQ) were calculated from the standard deviations of the data points found in Figure 25. The standard deviations of the resistance data for the blank (pH 5 exposed) were used in combination with the data fittings (A6) to find the LOD and sensitivity.

<i>Sensor type</i>	<i>Limit of Detection</i>	<i>Sensitivity</i>
<i>Type 1</i>	0.014 pH unit	0.18 pH unit
<i>Type 2</i>	0.033 pH unit	0.05 pH unit
<i>Type 2 PAN/PPy</i>	0.007 pH unit	0.01 pH unit

Table 8: Table showing the relevant Limit of Detection and Sensitivity performance metrics found according to the data from Figure 25.

The LOD and LLOQ determination methods are defined by IUPAC and theoretically calculated. To validate the use of LOD and LLOQ, an experimental approach was used. The electrical resistance response of type 2 PPy (higher RR) was tested for pH differences of 0.5 and 0.1. The sensing material was exposed to pH of 5 and 5.5 as well as 5 and 5.1 in alternating fashion. Type 2 PPy can successfully detect a 0.1 pH difference (Figure 26). The response is well within the range of 3 times the standard deviation which is the definition of LOD (Table 3). Alternating between pH 5, 5.5 and 8 exposure was performed additionally (A7, A8).

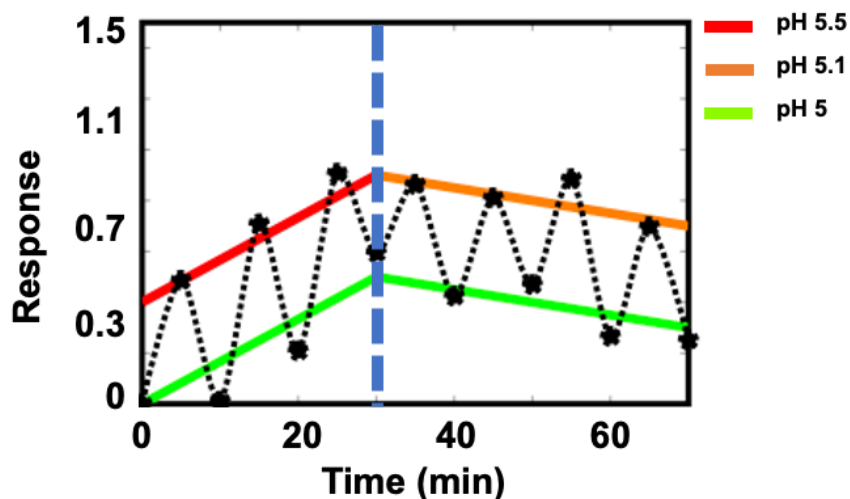


Figure 26: pH response of type 2 PPy sensing material where the response was analyzed alternating between pH 5 and 5.5 exposure. Subsequently, exposure to pH 5 and 5.1 solutions was performed alternately.

#### *Detection and Recovery Time*

The detection and recovery time, as well as the drift performance of all three sensing types produced were deduced from continuous resistance measurements using a DMM set up (Figure 11). pH 5 was considered the base point, subsequently increasing the pH in stepwise fashion, returning to pH 5 exposure before every increase. The continuous resistance measuring results are shown in Figure 27. The detection and recovery times were calculated from the results in Figure 27 according to the definitions from section 2.5 (Table 9). Stepwise (pH 5-9) continuous

resistance measurements without returning to pH 5 were performed additionally for type 1 and type 2 PPy sensing materials (A9, A10).

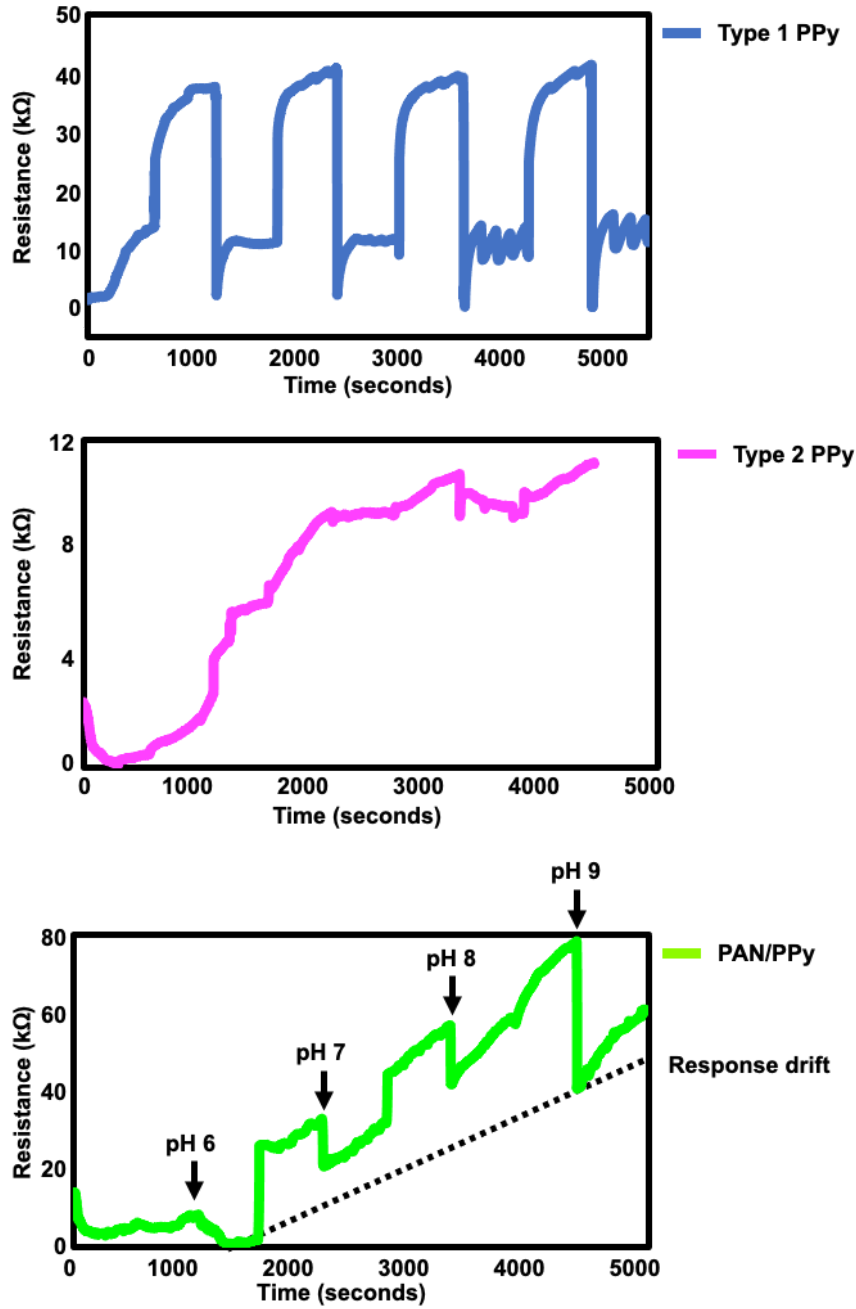


Figure 27: Graphical representation of the continuous resistance measurements performed experimentally using a DMM setup. The pH of the response points are shown for the nanofibrous PAN/PPy material as well as the electrical resistance response drift.

<b><i>Sensor type</i></b>	<b><i>Detection time (<math>t_D</math>) (seconds)</i></b>	<b><i>Recovery time (<math>t_R</math>) (seconds)</i></b>
<b><i>Type 1</i></b>	107	138
<b><i>Type 2</i></b>	126	199
<b><i>Type 2 PAN/PPy</i></b>	242	335

Table 9: Detection and recovery times associated with pH sensing types resulting from the DMM measurements in Figure 27, calculated according to the definitions in Table 3.

The continuous electrical resistance experiment results show drastic differences between the sensing material types (Figure 27). The Type 1 (RR 0.1) PPy curve has the lowest observed drift. Besides, differences in resistance response between pH 6 to pH 9 are barely observed. The expected trend of increasing electrical resistance with increasing pH not present. Type 1 curve shows an overshoot and oscillation observed in electrical resistance when returning to pH 5 exposure from higher pH solutions.

For the type 2 PPy (higher RR), the 4-point probe sheet resistance measurements of Figure 25 shows an increasing resistance response curve with pH. This is in alignment with the hypothesis that the deprotonation of PPy at increased pH influences the resistance of the PPy thin-film. There is, however, no observable correlation between the pH the material is exposed to and the resistance measured. Type 1 PPy (lower RR) has higher response differences compared to Type 2 (higher RR) PPy

For the PPy/PAN fibers, a clear correlation between the pH the sensor is exposed to and the resistance measured is observed. Although not linear, a response drift can be distinguished (Figure 27). The PPy/PAN shows better relationship between pH and resistance response and a higher sensitivity compared to type 2 PPy on a polycarbonate substrate.

It should be noted that there are considerable differences in the order of magnitude of the resistance response measured (Figure 27). The type 2 PPy sample has a maximum resistance response of only 15% of that of the electrospun PAN/PPy. This is in accordance with the results found by Bhattacharyya *et al.* on oCVD based nanofibrous sensor devices where higher electrical resistance differences are found for fibrous sensing material [94].

The resistance response of type 1 PPy has significantly higher electrical resistance changes compared to type 2 PPy. It could be that this is due to the relative amount of bipolaron complexes present. Figure 22 shows the proposed concentration of bipolaron complexes as well as the dopant concentration present in the system is significantly lower for type 1 PPy compared to type 2 PPy. A bipolaron unit from the conjugated chain (Figure 7) has a higher relative impact on the charge carrying capability of the PPy chain in type 1 PPy compared to type 2. Type 2 PPy has a higher concentration of bipolaron units so that the removal of a bipolaron unit has a less severe effect on the increase in electrical resistance measured.

For the performance metrics, the drift is not taken into account (Table 9). The type 2 PPy and the PAN/PPy nanofibrous materials do not show a linear drift response. Therefore, it is not possible to fit a linear drift curve. Besides, the type 2 PPy continuous resistance curve does not show a clear correlation between the pH it is exposed to and the resistance measured.

The 4-point probe results for type 2 PPy are in accordance with the expected resistance increase with pH (Figure 25). In contrast, the continuous curve shows no clear correlation (Figure 27). Although deemed to be of no influence, the effect of the silver paste and copper tape used in the

experimental setup of the DMM continuous experiments (Figure 11) needs to be examined further.

### *pH Sensing Performance*

The performance metrics of the oCVD-based PPy pH sensing materials are compared to current state-of-the-art literature-described pH biosensing devices. (Table 10). It can be seen that the pH range is in accordance with the pH range required for biomedical pH sensing. The response time is relatively slow but satisfactory for continuous pH biosensing in wound healing applications where fast pH sensing is not required (Figure 6). The PAN/PPy nanofibrous material possesses a very high-precision pH response where the limit of detection meets standards of state-of-the-art laboratory glass-electrode pH sensors [96]. The results indicate that vapor phase deposited PPy is suitable as a pH sensing material having a suitable limit of detection and pH sensing range for biomedical applications.

<i>Material</i>	<i>pH range</i>	<i>Response time</i>	<i>LOD</i>
PANI [97]	4-7	~ 60 s	-
PANI [98]	5.5-8	~ 20 s	-
PANI [99]	7.5-10.4	-	0.2 pH unit
Glass electrode [100]	-	-	0.1 pH unit
oCVD PPy (this work)	5-9	~ 107 s (type 1 PPy)	~0.007 pH unit (PAN/PPy)

Table 10: Overview of literature proposed pH biosensors compared to the oCVD PPy thin-film pH biosensor performance.

## **Conclusion**

The aim of this research was to exploit the characteristics of oCVD processing to overcome the limitations faced by other polymerization methods used to produce CPs for pH sensing applications. oCVD can provide increased conjugation length and control over the conjugation length. Besides, control over the dopant is improved. Furthermore, the processing ability, the ability to make defect-free ultrathin-films as well as the observed electrical conductivity is significantly enhanced using oCVD. oCVD processing of CP's can fill the gaps in biosensing application areas for pH sensing like wound healing where current devices lack design workability and applicational use. Polypyrrole was selected because its pH sensing range between pKa and pKb dissociation constants was best suited for physiological sensing. The use of polypyrrole thin-films produced by oCVD for pH sensing is examined where the conductometric performance of three distinctly different sensing materials were analyzed according to a set of performance metrics. It was found that the precision of the pH response of the PAN/PPy nanofibrous sensing material meets standards of laboratory-used glass electrode pH meters.

The gap in research in the understanding of the conductivity and corresponding structural changes in polypyrrole as a result of pH exposure was examined. A unique combination of analysis of the deprotonation due to pH exposure by UV-Vis, FT-IR and XPS with electrical resistance

measurements has been performed. An increasing band gap and decreasing conjugation length have been observed from the UV-Vis analysis. This decreasing conjugation length was further observed in the FT-IR spectrum. A similar inverse correlation between the dopant and bipolaron/polaron concentration with the electrical resistance was observed with XPS and FT-IR. The relation and interchangeability of the bipolarons and polarons is still not well understood. This research suggests that the decrease in bipolarons due to deprotonation is more severe than that of polarons. This suggested phenomenon is described by the effective polaron contribution increase with pH. This is found uniquely in oCVD processed polypyrrole. Experimental data indicates that this is due to the properties of the oCVD processing where exceptionally high conjugation length and dopant concentration PPy can be produced. The XPS data shows a decrease in both the bipolaron and polaron contributions with increasing pH with an increase in neutral R=N-R corresponding to the deprotonation of bipolaron units. This is further demonstrated by the decrease in presence of Cl<sup>-</sup> anions, related to stabilization of bipolaron/polaron units.

### ***Future Outlook***

The improved oCVD processability of CP's like polypyrrole opens the pathway for use in specialized sensor equipment tailored for specific (biomedical) sensing requirements. Further tailoring of oCVD produced PPy thin-films into a specialized pH sensor device for continuous pH monitoring can be done to serve specific application gaps of current pH monitoring such as wound healing, urine or sweat. Besides, sensor design and oCVD parameters can be examined to improve the performance metrics of the sensor. The precision (LOD) of the pH response of especially the PAN/PPy fibers displays it is able to challenge current glass electrode industrial pH meters precision. The use of PPy in sensing can be further explored with the detection of other types of analytes like glucose, glutamine or gasses.

The ratio of the bipolarons and polarons as well as their exact contribution to the deprotonation needs more research to further understand the corresponding deprotonation mechanism. More knowledge about this process could further broaden the application area of PPy into specific drug delivery applications with controlled dopant anion release and deprotonation in the PPy system.

### ***Acknowledgments***

I would like to express my gratitude to Advit Mukherjee. Besides training me on the CVD reactor and guiding me through the research project process, the brainstorming and discussions have led to great new insights and further research directions. I could not have done this research without her. I am vastly grateful to Prof Dr Ranjita K. Bose and Dr Ajay G.P. Kottapalli for their supervision of my research project and the fruitful meetings. It provided very helpful feedback and guided me through the research process.

XPS analysis was performed to analyze the deprotonation of PPy with different pH solutions. XPS was performed in collaboration with the Zernike Institute of Advanced Materials (ZIAM) surfaces and thin films research group at the University of Groningen. This could not have been done without the help and expertise of Dr H. Hemmatpour for which I am very thankful.

Thanks should go to Prof Dr F. Picchioni for lively discussions on research results. I am also grateful to Dr D. Sengupta for training me on electrospinning equipment. Besides, L. Rohrbach and G. Boer as lab technicians for helping me get acquainted with lab analytical techniques for which I am indebted.

Lastly, I would be remiss in not mentioning my family, friends and everyone from the study association G.T.D. Bernoulli for keeping my motivation high and supporting me in the process.

## ***Bibliography***

1. Das TK, Prusty S. Review on Conducting Polymers and Their Applications. *Polym Plast Technol Eng.* 2012;51: 1487–1500.
2. Fortunato E, Barquinha P, Martins R. Oxide semiconductor thin-film transistors: a review of recent advances. *Adv Mater.* 2012;24: 2945–2986.
3. Manuja A, Kumar B, Kumar R, Chhabra D, Ghosh M, Manuja M, et al. Metal/metal oxide nanoparticles: Toxicity concerns associated with their physical state and remediation for biomedical applications. *Toxicol Rep.* 2021;8: 1970–1978.
4. Dakshayini BS, Reddy KR, Mishra A, Shetti NP, Malode SJ, Basu S, et al. Role of conducting polymer and metal oxide-based hybrids for applications in amperometric sensors and biosensors. *Microchem J.* 2019;147: 7–24.
5. Zhang F, Johansson M, Andersson MR, Hummelen JC, Inganäs O. Polymer photovoltaic cells with conducting polymer anodes. *Adv Mater.* 2002;14: 662–665.
6. Zhao F, Shi Y, Pan L, Yu G. Multifunctional Nanostructured Conductive Polymer Gels: Synthesis, Properties, and Applications. *Acc Chem Res.* 2017;50: 1734–1743.
7. Diaz AF, Keiji Kanazawa K, Gardini GP. Electrochemical polymerization of pyrrole. *J Chem Soc Chem Commun.* 1979; 635–636.
8. Zhang Z, Rouabhia M, Moulton SE, editors. *Conductive Polymers: Electrical Interactions in Cell Biology and Medicine.* CRC Press; 2018.
9. Ansari R. Polypyrrole Conducting Electroactive Polymers: Synthesis and Stability Studies. *J Chem Chem Eng.* 3: 186–201.
10. Scott JC, Pfluger P, Krounbi MT, Street GB. Electron-spin-resonance studies of pyrrole polymers: Evidence for bipolarons. *Phys Rev B Condens Matter.* 1983;28: 2140–2145.
11. Awuzie CI. Conducting Polymers. *Materials Today: Proceedings.* 2017;4: 5721–5726.
12. Bhattacharya A, De A. Conducting Polymers in Solution—Progress Toward Processibility. *J Macromol Sci Part A Pure Appl Chem.* 1999;39: 17–56.
13. Kumar D, Sharma RC. Advances in conductive polymers. *Eur Polym J.* 1998;34: 1053–1060.
14. Hackett AJ, Malmström J, Travas-Sejdic J. Functionalization of conducting polymers for biointerface applications. *Prog Polym Sci.* 2017;70: 18–33.
15. Carrasco PM, Grande HJ, Cortazar M, Alberdi JM, Areizaga J, Pomposo JA. Structure–conductivity relationships in chemical polypyrroles of low, medium and high conductivity. *Synth Met.* 2006;156: 420–425.
16. Yang Y, Holdcroft S. Synthetic strategies for controlling the morphology of proton conducting polymer membranes. *Fuel Cells.* 2005;5: 171–186.

17. Jiang Y, Dong X, Sun L, Liu T, Qin F, Xie C, et al. An alcohol-dispersed conducting polymer complex for fully printable organic solar cells with improved stability. *Nature Energy*. 2022;7: 352–359.
18. Maisch P, Eisenhofer LM, Tam KC, Distler A, Voigt MM, Brabec CJ, et al. A generic surfactant-free approach to overcome wetting limitations and its application to improve inkjet-printed P3HT:non-fullerene acceptor PV. *J Mater Chem A Mater Energy Sustain*. 2019;7: 13215–13224.
19. Nejati S, Lau KKS. Chemical vapor deposition synthesis of tunable unsubstituted polythiophene. *Langmuir*. 2011;27: 15223–15229.
20. Dianatdar A, Miola M, De Luca O, Rudolf P, Picchioni F, Bose RK. All-dry, one-step synthesis, doping and film formation of conductive polypyrrole. *J Mater Chem*. 2022;10: 557–570.
21. Baughman RH, Shacklette LW. Conductivity as a function of conjugation length: Theory and experiment for conducting polymer complexes. *Phys Rev B Condens Matter*. 1989;39: 5872–5886.
22. Barr MC, Rowehl JA, Lunt RR, Xu J, Wang A, Boyce CM, et al. Direct monolithic integration of organic photovoltaic circuits on unmodified paper. *Adv Mater*. 2011;23: 3499–3505.
23. Stejskal J, Trchová M, Bober P, Morávková Z, Kopecký D, Vřhata M, et al. Polypyrrole salts and bases: superior conductivity of nanotubes and their stability towards the loss of conductivity by deprotonation. *RSC Adv*. 2016;6: 88382–88391.
24. Bonifas AP, McCreery RL. Solid state spectroelectrochemistry of redox reactions in polypyrrole/oxide molecular heterojunctions. *Anal Chem*. 2012;84: 2459–2465.
25. Lock JP, Im SG, Gleason KK. Oxidative Chemical Vapor Deposition of Electrically Conducting Poly(3,4-ethylenedioxythiophene) Films. *Macromolecules*. 2006;39: 5326–5329.
26. Heydari Gharahcheshmeh M, Gleason KK. Device fabrication based on oxidative chemical vapor deposition (oCVD) synthesis of conducting polymers and related conjugated organic materials. *Adv Mater Interfaces*. 2019;6: 1801564.
27. Lange U, Roznyatovskaya NV, Mirsky VM. Conducting polymers in chemical sensors and arrays. *Anal Chim Acta*. 2008;614: 1–26.
28. Wu X, Hou L, Lin X, Xie Z. Chapter 12 - Application of Novel Nanomaterials for Chemo- and Biosensing of Algal Toxins in Shellfish and Water. In: Wang X, Chen X, editors. *Novel Nanomaterials for Biomedical, Environmental and Energy Applications*. Elsevier; 2019. pp. 353–414.
29. Alqarni SA. A Review on Conducting Polymers for Colorimetric and Fluorescent Detection of Noble Metal Ions (Ag<sup>+</sup>, Pd<sup>2+</sup>, Pt<sup>2+/4+</sup>, and Au<sup>3+</sup>). *Crit Rev Anal Chem*. 2022; 1–12.
30. Alawsy T, Mattia GP, Al-Bawi Z, Beraldi R. Smartphone-based colorimetric sensor application for measuring biochemical material concentration. *Sensing and Bio-Sensing Research*. 2021;32: 100404.
31. Kudr J, Zitka O, Klimanek M, Vrba R, Adam V. Microfluidic electrochemical devices for pollution analysis—A review. *Sens Actuators B Chem*. 2017;246: 578–590.
32. Manjakkal L, Szwagierczak D, Dahiya R. Metal oxides based electrochemical pH sensors: Current progress and future perspectives. *Prog Mater Sci*. 2020;109: 100635.



33. Patil S, Ghadi H, Ramgir N, Adhikari A, Rao VR. Monitoring soil pH variation using Polyaniline/SU-8 composite film based conductometric microsensor. *Sens Actuators B Chem.* 2019;286: 583–590.
34. Unger K, Greco F, Coclite AM. Temporary tattoo pH sensor with pH-responsive hydrogel via initiated chemical vapor deposition. *Adv Mater Technol.* 2022;7: 2100717.
35. Choi J, Ghaffari R, Baker LB, Rogers JA. Skin-interfaced systems for sweat collection and analytics. *Sci Adv.* 2018;4: eaar3921.
36. Yue X, Xu F, Zhang L, Ren G, Sheng H, Wang J, et al. Simple, Skin-Attachable, and Multifunctional Colorimetric Sweat Sensor. *ACS Sens.* 2022;7: 2198–2208.
37. Yoon JH, Kim S-M, Park HJ, Kim YK, Oh DX, Cho H-W, et al. Highly self-healable and flexible cable-type pH sensors for real-time monitoring of human fluids. *Biosens Bioelectron.* 2020;150: 111946.
38. McLister A, McHugh J, Cundell J, Davis J. New Developments in Smart Bandage Technologies for Wound Diagnostics. *Adv Mater.* 2016;28: 5732–5737.
39. Lambers H, Piessens S, Bloem A, Pronk H, Finkel P. Natural skin surface pH is on average below 5, which is beneficial for its resident flora. *Int J Cosmet Sci.* 2006;28: 359–370.
40. Bennison LR, Miller CN, Summers RJ, Minnis AMB, Sussman G, McGuinness W. The pH of wounds during healing and infection: a descriptive literature review. *Wound Practice & Research: Journal of the Australian Wound Management Association.* 2017;25: 63–69.
41. Schreml S, Szeimies R-M, Karrer S, Heinlin J, Landthaler M, Babilas P. The impact of the pH value on skin integrity and cutaneous wound healing. *J Eur Acad Dermatol Venereol.* 2010;24: 373–378.
42. Frykberg RG, Banks J. Challenges in the Treatment of Chronic Wounds. *Adv Wound Care.* 2015;4: 560–582.
43. Jones EM, Cochrane CA, Percival SL. The Effect of pH on the Extracellular Matrix and Biofilms. *Adv Wound Care.* 2015;4: 431–439.
44. Schneider LA, Korber A, Grabbe S, Dissemond J. Influence of pH on wound-healing: a new perspective for wound-therapy? *Arch Dermatol Res.* 2007;298: 413–420.
45. Wilson IAI, Rd Q, Pj B, Others. The pH of varicose ulcer surfaces and its relationship to healing. 1979. Available: <https://pascal-francis.inist.fr/vibad/index.php?action=getRecordDetail&idt=PASCAL8050261407>
46. Gaohua L, Miao X, Dou L. Crosstalk of physiological pH and chemical pKa under the umbrella of physiologically based pharmacokinetic modeling of drug absorption, distribution, metabolism, excretion, and toxicity. *Expert Opin Drug Metab Toxicol.* 2021;17: 1103–1124.
47. Ahiabu A, Serpe MJ. Rapidly Responding pH- and Temperature-Responsive Poly (N-Isopropylacrylamide)-Based Microgels and Assemblies. *ACS Omega.* 2017;2: 1769–1777.
48. Yue F, Ngim TS, Hailin G. A novel paper pH sensor based on polypyrrole. *Sens Actuators B Chem.* 1996;32: 33–39.

49. Humpolíček P, Kašpárková V, Pacherník J, Stejskal J, Bober P, Capáková Z, et al. The biocompatibility of polyaniline and polypyrrole: A comparative study of their cytotoxicity, embryotoxicity and impurity profile. *Mater Sci Eng C Mater Biol Appl.* 2018;91: 303–310.
50. Wan H, Yang SC. Controlling the pKa for Protonic Doping of Polyaniline by Non-covalent Complexation. *MRS Online Proceedings Library.* 2007;965: 1223.
51. Mu S, Chen C, Xue H. ESR properties of polyaniline in a wide pH range. *J Electroanal Chem .* 2014;724: 71–79.
52. Sethumadhavan V, Zuber K, Bassell C, Teasdale PR, Evans D. Hydrolysis of doped conducting polymers. *Commun Chem.* 2020;3: 153.
53. van Lierop B, Castle L, Feigenbaum A, Boenke A. 2,5-Bis(5-tert-butyl-2-benzoxazolyl)thiophene. *Spectra for the Identification of Additives in Food Packaging.* Dordrecht: Springer Netherlands; 1998. pp. 54–58.
54. Ray SS, Gusain R, Kumar N, Ray SS, Gusain R, Kumar N. *Carbon Nanomaterial-Based Adsorbents for Water Purification: Fundamentals and Applications.* 2020.
55. Seike M, Uda M, Suzuki T, Minami H, Higashimoto S, Hirai T, et al. Synthesis of Polypyrrole and Its Derivatives as a Liquid Marble Stabilizer via a Solvent-Free Chemical Oxidative Polymerization Protocol. *ACS Omega.* 2022;7: 13010–13021.
56. Kaufman JH, Colaneri N, Scott JC, Street GB. Evolution of Polaron States into Bipolarons in Polypyrrole. *Physical Review Letters.* 1984. pp. 1005–1008. doi:10.1103/physrevlett.53.1005
57. Rumrill SM, Agarwal V, Lau KKS. Conformal Growth of Ultrathin Hydrophilic Coatings on Hydrophobic Surfaces Using Initiated Chemical Vapor Deposition. *Langmuir.* 2021;37: 7751–7759.
58. Wright SC, Fleck NA, Stronge WJ. Ballistic impact of polycarbonate—An experimental investigation. *Int J Impact Eng.* 1993;13: 1–20.
59. Al-Ahmed A, Mohammad F, Rahman MZA. Preparation, characterization, thermooxidative degradation, and stability of polyaniline/polyacrylonitrile composites in terms of direct-current electrical conductivity retention. *J Appl Polym Sci.* 2006;99: 437–448.
60. Bhardwaj N, Kundu SC. Electrospinning: a fascinating fiber fabrication technique. *Biotechnol Adv.* 2010;28: 325–347.
61. De Vrieze S, Van Camp T, Nelvig A, Hagström B, Westbroek P, De Clerck K. The effect of temperature and humidity on electrospinning. *J Mater Sci.* 2009;44: 1357–1362.
62. Gribkova OL, Nekrasov AA. Spectroelectrochemistry of Electroactive Polymer Composite Materials. *Polymers .* 2022;14. doi:10.3390/polym14153201
63. Smith BC. *Fundamentals of Fourier Transform Infrared Spectroscopy.* CRC Press; 2011.
64. Chastain J, King RC Jr. *Handbook of X-ray photoelectron spectroscopy.* Perkin-Elmer Corporation. 1992. Available: [https://www.researchgate.net/profile/Akif-Zeb/post/How\\_can\\_I\\_evaluate\\_at\\_of\\_N\\_in\\_TiO2\\_using\\_XPS\\_technique/attachment/5f3ebac4ce377e00016e3bc5/AS%3A926669195993088%401597946561045/download/MANXPS.pdf](https://www.researchgate.net/profile/Akif-Zeb/post/How_can_I_evaluate_at_of_N_in_TiO2_using_XPS_technique/attachment/5f3ebac4ce377e00016e3bc5/AS%3A926669195993088%401597946561045/download/MANXPS.pdf)

65. Leamy HJ. Charge collection scanning electron microscopy. *J Appl Phys.* 1982;53: R51–R80.
66. Kinder R, Mikolášek M, Donoval D, Kováč J, Tlaczala M. Measurement System with Hall and a Four Point Probes for Characterization of Semiconductors. *Journal of Electrical Engineering.* 2013;64: 106–111.
67. White RJ, Zhang B, Daniel S, Tang JM, Ervin EN, Cremer PS, et al. Ionic conductivity of the aqueous layer separating a lipid bilayer membrane and a glass support. *Langmuir.* 2006;22: 10777–10783.
68. Long GL, Winefordner JD. Limit of detection. A closer look at the IUPAC definition. *Anal Chem.* 1983;55: 712A–724A.
69. The International Union of Pure, (iupac) AC. Compendium of chemical terminology. [cited 7 Mar 2023]. Available: <https://goldbook.iupac.org/>
70. Kadian N, Raju KSR, Rashid M, Malik MY, Taneja I, Wahajuddin M. Comparative assessment of bioanalytical method validation guidelines for pharmaceutical industry. *J Pharm Biomed Anal.* 2016;126: 83–97.
71. Buck RP, Lindner E, Kutner W, Inzelt G. Piezoelectric chemical sensors (IUPAC Technical Report). *J Macromol Sci Part A Pure Appl Chem.* 2004;76: 1139–1160.
72. Mann U. Principles of Chemical Reactor Analysis and Design: New Tools for Industrial Chemical Reactor Operations. Wiley; 2009.
73. Kim DY, Lee JY, Moon DK, Kim CY. Stability of reduced polypyrrole. *Synth Met.* 1995;69: 471–474.
74. Osaka T, Momma T, Komaba S-I, Kanagawa H, Nakamura S. Electrochemical process of formation of an insulating polypyrrole film. *J Electroanal Chem.* 1994;372: 201–207.
75. Ullah H, Shah A-U-HA, Bilal S, Ayub K. Doping and Dedoping Processes of Polypyrrole: DFT Study with Hybrid Functionals. *J Phys Chem C.* 2014;118: 17819–17830.
76. Shiigi H, Kishimoto M, Yakabe H, Deore B, Nagaoka T. Highly selective molecularly imprinted overoxidized polypyrrole colloids: one-step preparation technique. *Anal Sci.* 2002;18: 41–44.
77. Brédas JL, Thémans B, André JM. Bipolarons in polypyrrole chains. *Phys Rev B Condens Matter.* 1983;27: 7827–7830.
78. Davidson RG, Turner TG. An IR spectroscopic study of the electrochemical reduction of polypyrrole doped with dodecylsulfate anion. *Synth Met.* 1995;72: 121–128.
79. Lamprakopoulos S, Yfantis D, Yfantis A, Schmeisser D, Anastassopoulou J, Theophanides T. An FTIR study of the role of H<sub>2</sub>O and D<sub>2</sub>O in the aging mechanism of conductive polypyrroles. *Synth Met.* 2004;144: 229–234.
80. Duchet J, Legras R, Demoustier-Champagne S. Chemical synthesis of polypyrrole: structure–properties relationship. *Synth Met.* 1998;98: 113–122.
81. Tabačiarová J, Mičušík M, Fedorko P, Omastová M. Study of polypyrrole aging by XPS, FTIR and conductivity measurements. *Polym Degrad Stab.* 2015;120: 392–401.

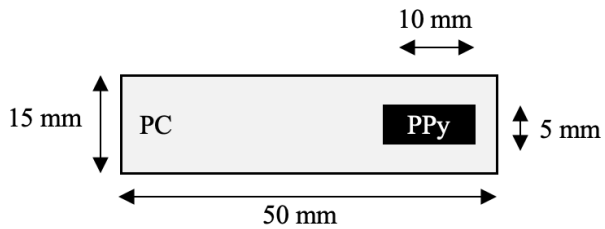
82. Blinova NV, Stejskal J, Trchová M, Prokeš J, Omastová M. Polyaniline and polypyrrole: A comparative study of the preparation. *Eur Polym J.* 2007;43: 2331–2341.
83. Rawal I, Goyal PK. Effect of Ammonia Based Deprotonation on the variable range hopping conduction in Polypyrrole Nanotubes. *Solid State Sci.* 2020;99: 105984.
84. Omastová M, Mosnáčková K, Trchová M, Konyushenko EN, Stejskal J, Fedorko P, et al. Polypyrrole and polyaniline prepared with cerium(IV) sulfate oxidant. *Synth Met.* 2010;160: 701–707.
85. Christensen PA, Hamnett A. In situ spectroscopic investigations of the growth, electrochemical cycling and overoxidation of polypyrrole in aqueous solution. *Electrochim Acta.* 1991;36: 1263–1286.
86. Genoud F, Guglielmi M, Nechtschein M, Genies E, Salmon M. ESR study of electrochemical doping in the conducting polymer polypyrrole. *Phys Rev Lett.* 1985;55: 118–121.
87. Pecher J, Mecking S. Nanoparticles of Conjugated Polymers. *Chem Rev.* 2010;110: 6260–6279.
88. Tian B, Zerbi G. Lattice dynamics and vibrational spectra of pristine and doped polypyrrole: Effective conjugation coordinate. *J Chem Phys.* 1990;92: 3892–3898.
89. Castiglioni C, Lopez Navarrete JT, Zerbi G, Gussoni M. A simple interpretation of the vibrational spectra of undoped, doped and photoexcited polyacetylene: Amplitude mode theory in the GF formalism. *Solid State Commun.* 1988;65: 625–630.
90. Lei J, Cai Z, Martin CR. Effect of reagent concentrations used to synthesize polypyrrole on the chemical characteristics and optical and electronic properties of the resulting polymer. *Synth Met.* 1992;46: 53–69.
91. Pei Q, Qian R. Protonation and deprotonation of polypyrrole chain in aqueous solutions. *Synth Met.* 1991;45: 35–48.
92. Malitesta C, Losito I, Sabbatini L, Zambonin PG. New findings on polypyrrole chemical structure by XPS coupled to chemical derivatization labelling. *J Electron Spectrosc Relat Phenom.* 1995;76: 629–634.
93. Saoudi B, Jammul N, Chehimi MM, Jaubert A-S, Arkam C, Delamar M. XPS study of the adsorption mechanisms of DNA onto polypyrrole particles. *Spectrosc Int J.* 2004;18: 519–535.
94. Bhattacharyya D, Senecal K, Marek P, Senecal A, Gleason KK. High surface area flexible chemiresistive biosensor by oxidative chemical vapor deposition. *Adv Funct Mater.* 2011;21: 4328–4337.
95. Fong H, Chun I, Reneker DH. Beaded nanofibers formed during electrospinning. *Polymer.* 1999;40: 4585–4592.
96. Mettler-Toledo International Inc. all rights reserved. PH buffer accuracy – comparison study. In: Mettler-Toledo International Inc. all rights reserved [Internet]. 8 Nov 2017 [cited 4 Apr 2023]. Available: <https://www.mt.com/ca/en/home/library/tips-and-tricks/lab-analytical-instruments/comparison-ph-buffer-accuracy.html>

97. Lee H, Song C, Hong YS, Kim M, Cho HR, Kang T, et al. Wearable/disposable sweat-based glucose monitoring device with multistage transdermal drug delivery module. *Sci Adv.* 2017;3: e1601314.
98. Guinovart T, Valdés-Ramírez G, Windmiller JR, Andrade FJ, Wang J. Bandage-based wearable potentiometric sensor for monitoring wound pH. *Electroanalysis.* 2014;26: 1345–1353.
99. Lindfors T, Ivaska A. Application of raman spectroscopy and sequential injection analysis for pH measurements with water dispersion of polyaniline nanoparticles. *Anal Chem.* 2007;79: 608–611.
100. Xu ZW, Zheng GL. Implementation of a high-precision pH sensor. *Appl Mech Mater.* 2013;373-375: 358–362.
101. Zargham S, Bazgir S, Tavakoli A, Rashidi AS, Damerchely R. The Effect of Flow Rate on Morphology and Deposition Area of Electrospun Nylon 6 Nanofiber. *J Eng Fiber Fabr.* 2012;7: 155892501200700414.

## Appendices

<i>Spin Coating Parameters</i>	<i>PAN</i>	<i>PVA</i>
Spinning type	Static	Static
Spinning speed	2500 rpm	2000 rpm
Spinning time	45 seconds	45 seconds

A1: Table showing spin coating parameters corresponding to the type of thin-film substrate produced for oCVD area selectivity analysis.



A2: Schematic representation of sizing of solid film PC with deposited PPy as sensor testing complex.

<i>pH of solution</i>	<i>Conductivity of solution (<math>\mu\text{S}/\text{cm}</math>)</i>
5	31.46
6	18.82
7	16.67
8	11.66
9	16.68
10	15.86
11	80.04
PPy thin film	5E3 - 2E5

A3:: Conductivity of pH solutions in comparison to the conductivity of the PPy thin film measured.

<i>Sample No.</i>	<i>Voltage applied (kV)</i>	<i>Flow rate (mL/hr)</i>	<i>Tip-to-collector distance</i>	<i>PAN/DMF wt. %</i>	<i>Mean Fiber diameter (<math>\mu\text{m}</math>)</i>
1	15	1	10 cm	10 wt%	0.948
2	11	1	10 cm	10 wt%	0.977
3	17	2	10 cm	10 wt%	0.983
4	19	2	10 cm	10 wt%	1.119
5	11	0.5	10 cm	10 wt%	1.328

A4: Table showing electrospinning parameters tested and subsequent mean fiber diameter measured. Mean fiber diameters were calculated as the mean of 100 fibers analyzed for their thickness. Survey performed at 21°C and 55% relative humidity. It is generally accepted that higher flow rate results in thicker fibers which in contrast is not observed in this survey comparing sample 2 to sample 5 [101]. Sample 5 parameters were used for free-standing fiber formation. Mean fiber diameters found using ImageJ software from 100 fiber diameter measurements.

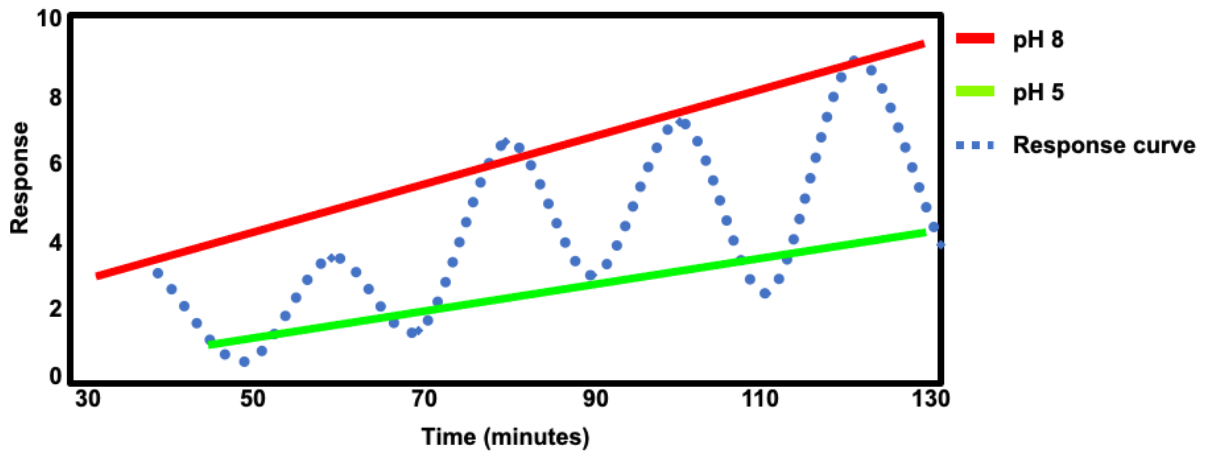
<i>oCVD parameters</i>	<i>oCVD conditions</i>
<i>Reaction temperature</i>	40 °C
<i>Pyrrole monomer flow rate</i>	2.5 cm <sup>3</sup> /min
<i>SbCl<sub>5</sub> oxidant flow rate</i>	0.5 cm <sup>3</sup> /min
<i>N<sub>2</sub> patch-flow rate</i>	10 m <sup>3</sup> /min
<i>Deposition pressure</i>	300 mTorr
<i>Deposition time</i>	15 min

A5: Table showing the reaction conditions used for the oCVD reaction of PPy using PAN nanofibers as substrate.

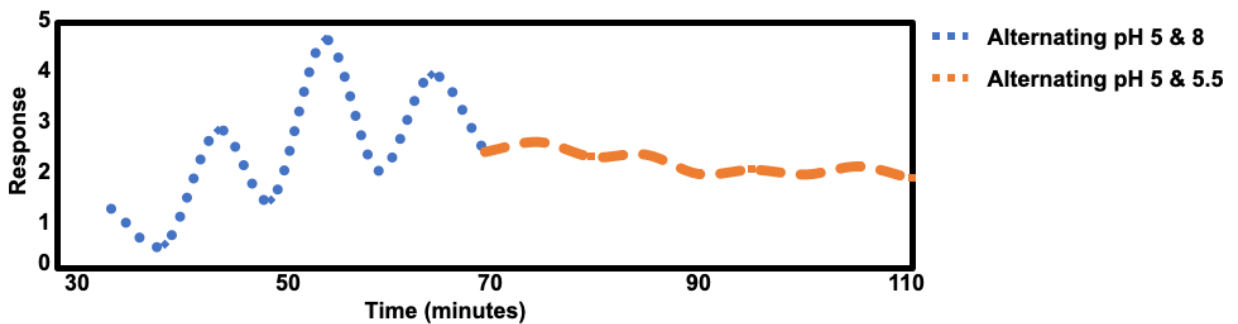
Sensor type	Curve Fitting	R <sup>2</sup> value
Type 1	$Response = -0.22911x^2 + 3.7299x - 12.756$	0.9339
Type 2	$Response = 0.9297x^2 - 10.656x + 30.352$	0.9973

PAN/PPy nanofibrous	$Response = 0.4464x^2 - 2.9746x + 3.2487$	0.9831
---------------------	---	--------

A6: Table showing the curve fittings for the response performance shown in Figure 25.

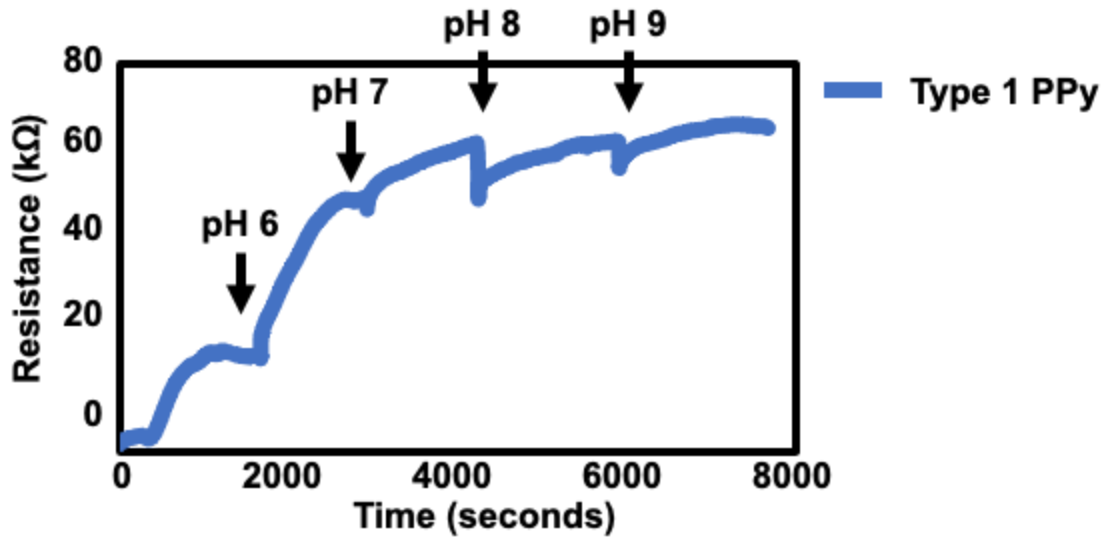


A7: Graphical representation of a type 2 PPy exposed to alternating pH 5 and pH 8 solutions. Relative response is shown as a function of the exposure time.

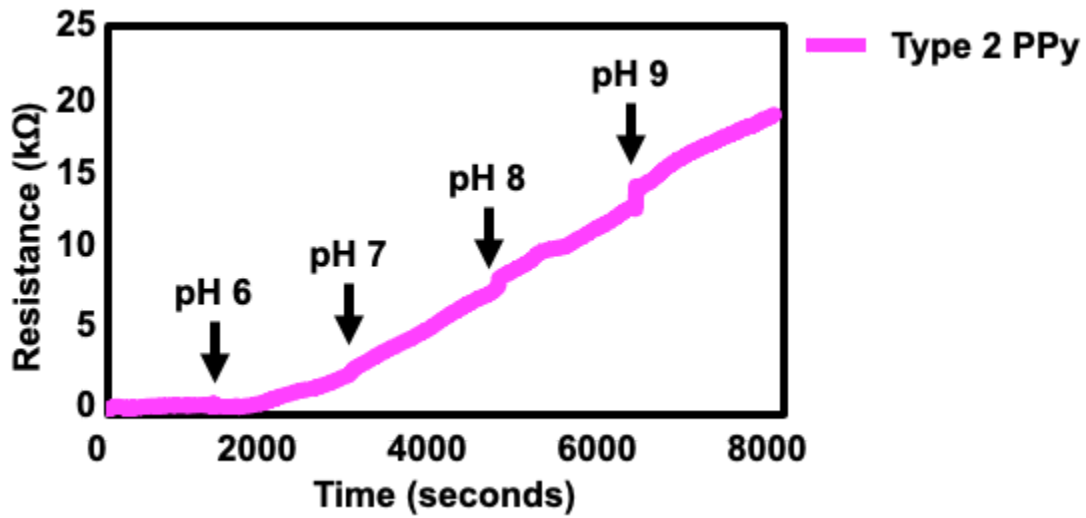


A8: Graphical representation of a type 2 PPy exposed to alternating pH 5 and pH 8 solutions (blue) followed by alternating pH 5 and 5.5 exposure (orange). Relative response is shown as a function of the exposure time.

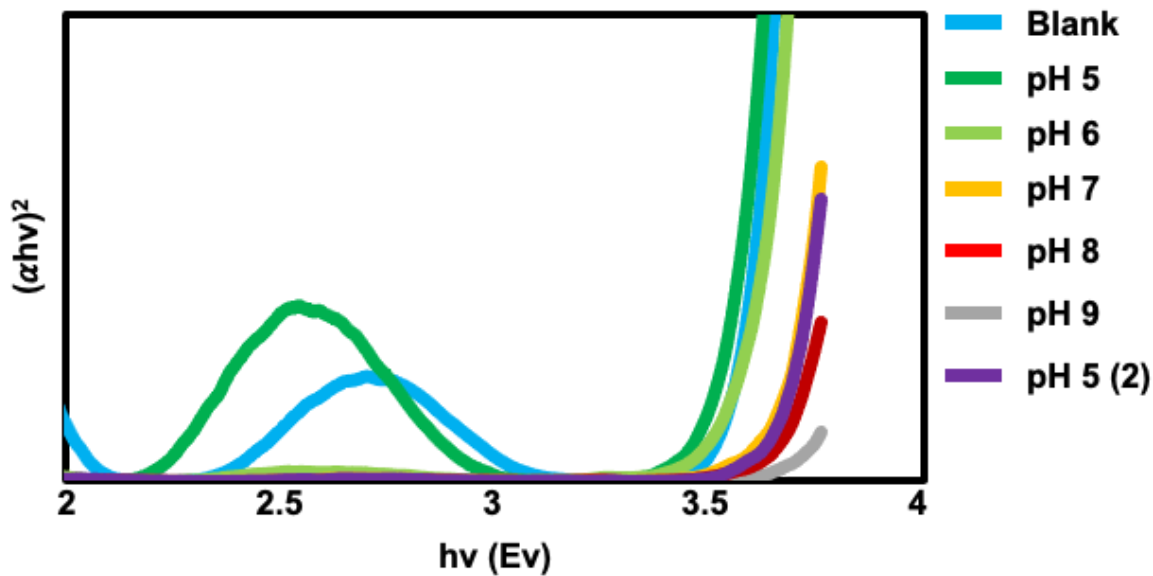




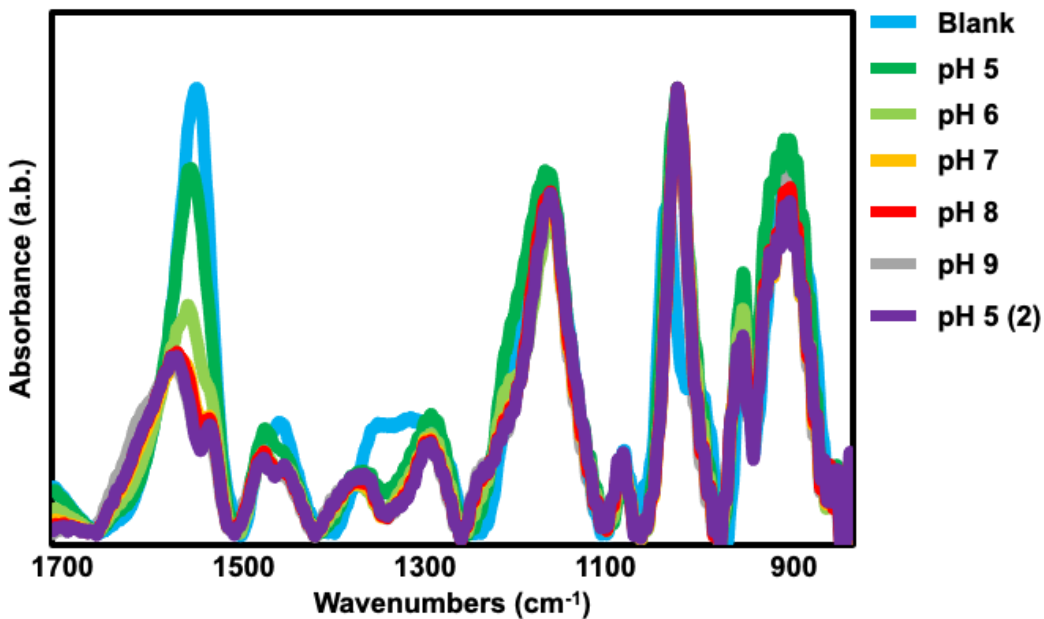
A9: graphical representation of the type 1 PPy exposed to different pH solutions using a DMM resistance measuring set-up.



A10: graphical representation of the type 2 PPy exposed to different pH solutions using a DMM resistance measuring set-up.



A11: Tauc plot for PPy exposed to different pH solutions. Band gap energies were found from a fit of the linear part of the spectra around 3.5 eV.



A12: full FT-IR spectrum of PPy thin-film on IR-transparent silicon wafer exposed to increasing pH solutions for 15 minutes. Exposure pH 5 (2) was performed after exposure to all previous pH.